https://doi.org/10.5194/egusphere-2023-2141
Preprint. Discussion started: 16 October 2023

Reorganisation of subglacial drainage processes during rapid melting of the Fennoscandian Ice Sheet

Adam J. Hepburn[1*], Christine F. Dow[1], Antti Ojala[2], Joni Mäkinen[2], Elina Ahokangas[2], Jussi Hovikoski[3], Jukka-Pekka Palmu[3], and Kari Kajuutti[2]

[1]Department of Geography and Environmental Management, University of Waterloo, Waterloo, ON, Canada
[2]Department of Geography and Geology, University of Turku, Turku, Finland
[3]Geological Survey of Finland, Espoo, Finland

Correspondence: Adam J. Hepburn, now at the European Space Astronomy Centre, European Space Agency, Madrid, Spain (adam.hepburn@esa.int)

Abstract. Unknown basal characteristics limit our ability to simulate the subglacial hydrology of rapidly thinning contemporary ice sheets. Subglacial water is typically conceptualised as being routed through either distributed, inefficient, and high-pressure systems, or channelised, efficient, and low-pressure systems, transitioning between the two as a function of discharge. Sediment-based landforms generated beneath Pleistocene ice sheets, together with detailed digital elevation models, offer a valuable means of parameterising and testing models of subglacial hydrology. However, previous work using geomorphology to inform modelling has concentrated on landforms relating to channelised drainage (e.g., eskers) while using inherently channelised models unable to capture transitions in drainage state. Landscapes relating to the distributed drainage system, and the hypothesised transitional zone of drainage between distributed and channelised drainage modes have therefore been largely ignored. To address this, we use the Glacier Drainage System model (GlaDS), a 2D finite element model capable of capturing the transition between distributed and channelised drainage, to explore the genesis of 'murtoos', a distinctive triangular landform found in murtoo fields throughout Finland and Sweden. Murtoos are hypothesised to form 40–60 km from the former Fennoscandian ice margin at the onset of channelised drainage where water pressure is at or exceeds ice overburden pressure. Concentrating within a specific ice lobe of the former Fennoscandian Ice Sheet and parameterised using digital elevation models with a simulated former ice surface geometry, we carried out a range of sensitivity testing to explore murtoo genesis and drainage transitions beneath the palaeo ice sheet. Our modelling supports many of the predictions for murtoo origin, including the location of water pressures equal to ice overburden, the onset of channelised drainage, and the predicted water depths in terrain surrounding murtoo fields. Modelled channels also closely match the general spacing, direction and complexity of eskers and mapped meltwater routes. Our results demonstrate that examining palaeo basal topography alongside subglacial hydrology model outputs holds promise for mutually beneficial analyses of palaeo and contemporary ice sheets to assess the controls of hydrology on ice dynamics and subglacial landform evolution.

https://doi.org/10.5194/egusphere-2023-2141
Preprint. Discussion started: 16 October 2023

1 Introduction

Surface melt delivered to the bed of glaciers and ice sheets exerts a strong but non-linear control on ice flow and mass loss (Schoof, 2010; Meierbachtol et al., 2013; Nienow et al., 2017; Davison et al., 2019; Wallis et al., 2023). At the onset of the melt-season, summer ice velocity speed-ups of between 10–300% relative to winter averages have been observed extending 10s of kilometres inland from marine (Sole et al., 2011; Joughin et al., 2008) and terrestrially terminating (Bartholomew et al., 2012) portions of the Greenland (Sole et al., 2013; Moon et al., 2014) and Antarctic ice sheets (Wallis et al., 2023; Tuckett et al., 2019). The basal hydrological system is primarily responsible for modulating the velocity response of glaciers to melt and is typically conceptualised as as existing in either i) an inefficient, *distributed* state in which water is transmitted through thin films (Weertman, 1972), linked-cavities (Kamb, 1987), or as Darcian flow through a porous medium (Boulton and Jones, 1979); or ii) an efficient, *channelised* system in which water is routed through Nye channels eroded down into the underlying substrate (Nye, 1972) or Röthlisberger channels (R-Channels, Röthlisberger, 1972) and Hooke channels (Hooke, 1989) formed within the ice itself. Below a critical threshold, increased discharge close to the ice margin (e.g., at the onset of a melt season) raises water pressure and lowers the frictional resistance to ice flow (Schoof, 2010). However, beyond this critical threshold, sustained high discharge and turbulent flow leads to wall-melt and channelisation (Hooke, 1989). This can lower the effective pressure, dampening the velocity response to meltwater input as water is increasingly routed through the efficient system (Iken and Bindschadler, 1986; Iverson et al., 1999; Schoof, 2005). The transition between inefficient and efficient modes of drainage throughout the melt season has important implications for ice sheet dynamics in a warming climate (see Greenwood et al., 2016; Nienow et al., 2017; Davison et al., 2019, for detailed reviews).

An accurate representation of basal hydrology in models is critical in efforts to predict the rate and timing of polar ice sheet mass loss. Models of basal hydrology have been widely used to investigate subglacial drainage beneath contemporary ice sheets (e.g., Schoof, 2005, 2010; Banwell et al., 2013; Werder et al., 2013; Flowers, 2018; Dow et al., 2022; Indrigo et al., 2021). However, despite recent work in both one and two-way coupling of basal-hydrology models to ice flow models (e.g., Cook et al., 2019, 2020, 2022; Ehrenfeucht et al., 2023), detailed treatment of basal hydrology is not yet widely integrated into ice sheet system models and predicting the rate and timing of glacial mass loss remains difficult (Dow, 2023). The response of ice flow to future melt depends on not only the volume, timing and duration of melt, but also critically, on the basal topography, underlying geology, and hydraulic properties of the subsurface material (Werder et al., 2013). Yet our knowledge of basal topography is limited to spatial resolutions in the order of 10^2 m (e.g., Morlighem et al., 2017, 2020) and direct observations of hydraulic connectivity are sparse, especially at the ice sheet scale (Greenwood et al., 2016). Boreholes and instrumentation placed within and beneath ice are one means of direct observation of hydraulic properties (e.g., Hubbard et al., 1995; Mair et al., 2003; Meierbachtol et al., 2013; Doyle et al., 2018, 2022), however, these are difficult to implement and impractical to use beyond a handful of sites per field campaign. Instead, much of our insight into subglacial hydrology has come from indirect proxies for drainage efficiency including proglacial discharge (e.g., Willis et al., 1996; Cowton et al., 2013), geophysical investigation (e.g., Chu et al., 2016; Killingbeck et al., 2020), and ice surface velocity time-series analysis (e.g., Mair et al., 2002; Tuckett et al., 2019; Wallis et al., 2023) from which the influence of channelised drainage has been inferred extending up to 50 km

https://doi.org/10.5194/egusphere-2023-2141
Preprint. Discussion started: 16 October 2023

inland of the Greenland Ice Sheet (GrIS) margin (Sole et al., 2013; Chandler et al., 2013, 2021). Without a strong control on the bed characteristics beneath contemporary ice sheets, estimating and defining an appropriate set of basal parameters remains a fundamental challenge to the accurate representation of basal hydrology in ice sheet models (Dow et al., 2020; Doyle et al., 2022; Hager et al., 2022; McArthur et al., 2023).

To this end, without overlying ice-cover, fluvioglacial landforms deposited beneath Pleistocene ice sheets may provide crucial information for the parameterisation of basal hydrological models during periods of rapid ice loss (e.g., Clark and Walder, 1994; Cofaigh, 1996; Rampton, 2000; Utting et al., 2009; Ojala et al., 2019; Coughlan et al., 2020; Dewald et al., 2022, 2021). Indeed, across both Europe and North America, eskers, tunnel valleys, and meltwater routes are nearly ubiquitous in many places (e.g., Brennand, 2000; Storrar et al., 2014; Storrar and Livingstone, 2017; Lewington et al., 2019; Kirkham et al., 2022). The distributed drainage system is less commonly described in landform records (Greenwood et al., 2016), although drumlin and ribbed formation likely represents flow instabilities associated with the high effective pressures within a distributed system (Fowler, 2010; Fowler and Chapwanya, 2014; Stokes et al., 2013; Chapwanya et al., 2011). Pleistocene eskers are often tens to hundreds of kilometres long (Storrar and Livingstone, 2017) and although similarly large channelised systems have been described in Antarctica (Dow et al., 2022), the ubiquity and scale of channelised drainage in the palaeo record is beyond the scale of channelised drainage typically described beneath the contemporary ice sheets. This, together with uncertainty surrounding their formation (Cofaigh, 1996; Greenwood et al., 2016), has largely limited the use of eskers to ice-flow direction indicators in empirical ice sheet reconstructions.

Work that has combined geomorphology with basal hydrology modelling has typically done so while making simplifying assumptions about the pressure water exists at, prescribing a fixed water pressure at or near overburden everywhere (e.g., Livingstone et al., 2013a, b, 2015; Karlsson and Dahl-Jensen, 2015; Shackleton et al., 2018; Kirkham et al., 2022). Although these assumptions are thought to hold over interannual scales, these models are inherently channelised and are unable to capture dynamic changes between distributed and channelised drainage (Banwell et al., 2013). To date, no work has explored the potential for palaeo beds to provide meaningful information regarding basal hydrological processes operating at the sub-annual scale and across the distributed–channelised transition, despite the need to better constrain hydrological models at these scales during periods of rapid climate change (Dow, 2023).

In this paper, we focus on a recently described feature termed ‘murtoos’ (singular: murtoo Mäkinen et al., 2017; Ojala et al., 2019)—low relief ($\sim$5 m) features with a distinctive, broadly triangular, morphology (Figure 1, Ojala et al., 2019; Ahokangas et al., 2021; Becher and Johnson, 2021; Ojala et al., 2021; Vérité et al., 2022; Van Boeckel et al., 2022). Initially identified from LiDAR data in Finland (Mäkinen et al., 2017) and Sweden (Peterson et al., 2017), murtoos have since been extensively mapped throughout terrain formerly occupied by the Fennoscandian Ice Sheet (FIS) (Ojala et al., 2019; Ahokangas et al., 2021). Regional mapping in Finland has demonstrated a preferential clustering of murtoo fields along meltwater routes—integrated networks of landforms associated with subglacial meltwater (Dewald et al., 2022)—which are in turn concentrated in more dynamic, *warm-based* sectors of the FIS including ice stream tracts, interlobate joints, and ice-stream confluence zones (Ahokangas et al., 2021; Palmu et al., 2021). Topographically, the murtoo formation environment is associated with subglacial

https://doi.org/10.5194/egusphere-2023-2141
Preprint. Discussion started: 16 October 2023

lake basins, bedrock depressions, and the lee side of some large bedrock protrusions (Ojala et al., 2021; Ahokangas et al., 2021).

Murtoos are absent within more passive, *cold-based* regions of the FIS (Ahokangas et al., 2021). In this way, murtoo distribution mimics that of eskers, ribbed moraines, drumlins, and other lineated features in Finland (Palmu et al., 2021). Murtoo fields are often closely associated adjacent to or downstream of drumlin fields, some are co-located amongst or downstream of ribbed moraines (e.g., Vérité et al., 2022, and Figure 1C), and murtoo fields may be located upstream of, and transition into, eskers (Figure 1D Ahokangas et al., 2021). Murtoos are hypothesised to form in a transitional zone between inefficient, distributed drainage networks, and the efficient, channelised drainage networks (Ojala et al., 2019). The close association of landforms relating to channelised drainage with murtoo routes may therefore mark the spatial and/or temporal transition to semi-distributed drainage and an excess of meltwater in areas subject to repeated and brief pulses of meltwater delivered to the bed during the rapid deglaciation of the FIS (Ojala et al., 2019, 2021; Ahokangas et al., 2021; Becher and Johnson, 2021; Ojala et al., 2022; Vérité et al., 2022; Mäkinen et al., 2023). Crucially, murtoos have a characteristic distribution, rarely closer than 40–60 km from the FIS margin at $\sim$12 $\mathrm{cal.\ ka}$ (Mäkinen et al., 2023), aligning well with the apparent limits of channelisation to within 50 km of the ice sheet margin in contemporary Greenland (Chandler et al., 2013, 2021).

Internal excavations within individual murtoos (e.g., Becher and Johnson, 2021; Mäkinen et al., 2023; Hovikoski et al., 2023) have revealed that murtoos consist of a core unit containing sorted sediments, overlain by a main body unit (referred to as Unit 2 by Mäkinen et al., 2023) that i) distally is comprised of alternating facies of heterogeneous diamicton, with strong fabrics interbedded with sorted gravelly and sandy sediment and ii) proximally, of glaciofluvial deposits, such as current ripples, transitional cross-bedding, and antidunal sinusoidal laminations reflecting alternating lower and upper flow regimes (Becher and Johnson, 2021; Mäkinen et al., 2023; Hovikoski et al., 2023). The murtoo body is, in turn, overlain by a mantling deposit heavily modified by soil forming processes, but nonetheless exhibiting weakly stratified diamicton and gravel beds as well as large boulders deposited by the ice-bed interface (Mäkinen et al., 2023). This sequence of sedimentological architecture suggest a murtoo body may form within a single melt season tracking the development of a semi-distributed drainage system:

1. In the first stage of murtoo formation, the sorted sediment dominated core develops following sediment deposition within a rapidly enlarging broad and shallow subglacial conduit—possibly associated with pre-existing till ridges or cavities in the lee-side of protrusions. Sediment within this core evidences at least partial ice contact, and is superposed over existing, meltwater route deposits (Mäkinen et al., 2023).

2. With the onset of spring melt, the murtoo body is deposited within an increasingly large conduit, promoting the deposition of sand lenses, sinusoidally stratified sand, and poorly-sorted gravel, with silt commonly draping ripple-scale features. In this phase of formation, cobbles are the largest clast size, which places an upper limit on water depth of $\sim$ 25 cm (Hovikoski et al., 2023). Subdivisions within this unit separated by muddy glaciofluvial deposits may relate to distinct peaks in meltwater input throughout the season (Mäkinen et al., 2023).

https://doi.org/10.5194/egusphere-2023-2141
Preprint. Discussion started: 16 October 2023

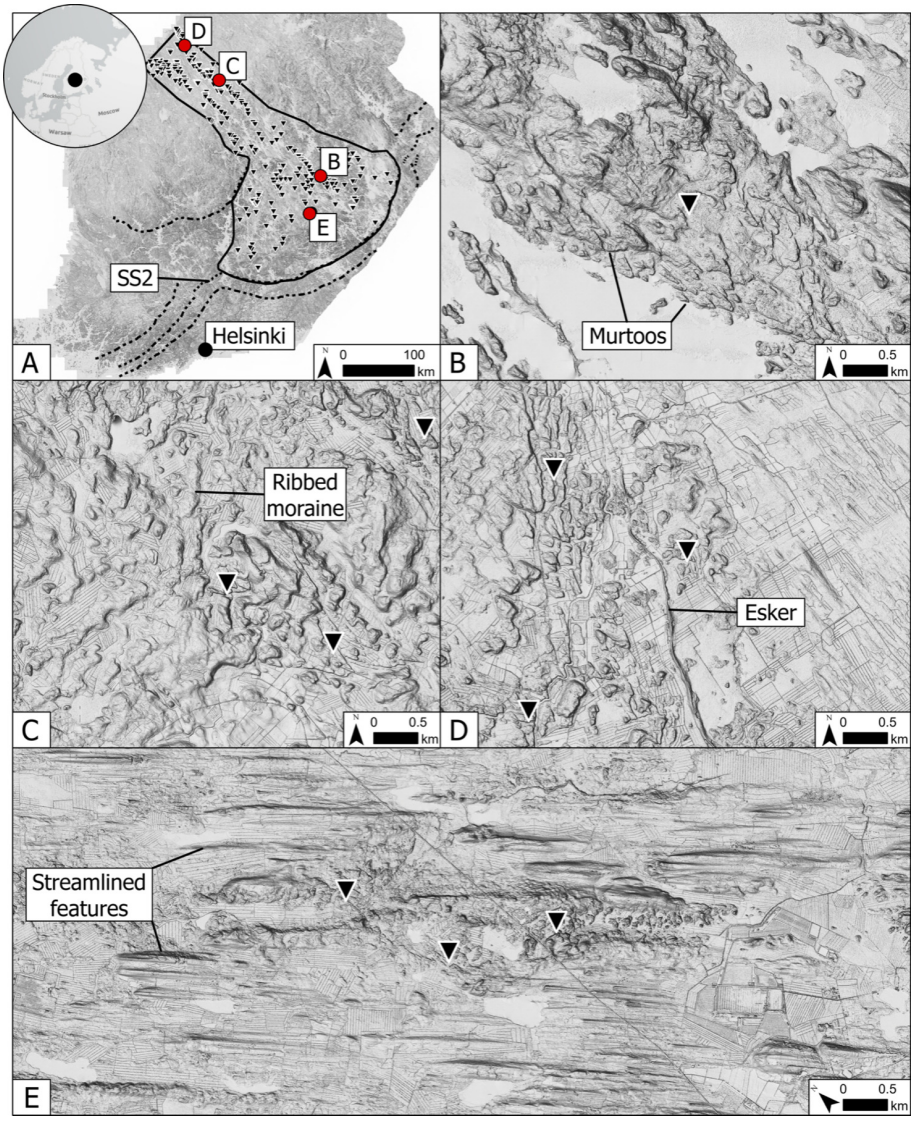

Figure 1. The study site. **A**) The extent of the GlaDS model domain (solid line) in the Finnish Lake District Ice Lobe (FLDIL) and the Salpausselkäs (dashed line). Salpausselkä II (SS2) marks the 12 cal. ka ice extent. Murtoo fields Ahokangas et al. (2021) within the FLDIL are shown as inverted triangles. **B**) A murtoo field visible in LiDAR data. Adjacent to the murtoos, a large esker is visible in the lake. **C**) Murtoo fields amongst ribbed moraines in the north of the FLDIL. **D**) An abrupt downstream transition from murtoo fields to a large esker. Additional murtoo fields are found directly adjacent to the esker. **E**) Three murtoo fields amongst streamlined terrain within at the centre of the FLDIL. Ice flow is from the upper left in all panels, with the exception of panel **E** in which ice flow is left to right.

https://doi.org/10.5194/egusphere-2023-2141
Preprint. Discussion started: 16 October 2023

3. As the melt season continues through summer, the increasing grain size indicates higher water velocity and depth accompanying the development of an enlarged pond. Sediments and boulder size-distributions on the upper slope appear consistent with upper-flow-regime deposits in which water depth neared 1 m (Hovikoski et al., 2023).

4. The development of this enlarged cavity/pond and subsequent pressure drop encourages localised creep closure at the broadest part of the murtoo, evidenced by a disappearance of sorted sediment, and in some murtoos this is succeeded by compacted diamicton–indicating ice-bed recoupling (Mäkinen et al., 2023). Meanwhile, closer to the margins of the murtoo body, meltwater flow continued and forced to pass an enclosed space, is routed obliquely towards the tip, forming boulder-rich proto-channels. These deposits indicate that the ice-bed recoupling coincided with intense and increasingly erosional channelised flow. The final stage of murtoo development is commonly represented by marginal channels that finalise the triangular shape of the murtoos (Becher and Johnson, 2021). The murtoo deposition is abruptly terminated as evidenced by sudden appearance of laminated mud deposited via suspension settling in the top of the marginal channels in some murtoos (Hovikoski et al., 2023). The overall increase in meltwater and sudden decay suggests murtoo development within a single melt season or rapid reorganisation associated with autogenic changes within the wider meltwater system (Hovikoski et al., 2023; Mäkinen et al., 2023).

Murtoo excavation indicates that murtoos are composite landforms arranged parallel to ice flow, comprising of a main body that is primarily depositional together with lateral margins and a lee-side head that are erosional forms. Together with murtoo mapping, this indicates that murtoos are formed subglacially amongst a network of low canals, conduits, or cavities in which water velocity is highly variable (Mäkinen et al., 2023). The interbedding of silt and clay poor sandy/gravelly diamictons with poorly sorted sediments are suggested to result from pulsed, sediment rich flows, and the limited evidence for glaciotectonic deformation suggests effective pressures close to zero (Mäkinen et al., 2023).

The short timescales over which murtoos are hypothesised to form, their small size, and their location at the onset of channelisation make them potentially important components of the subglacial system, and ideal geomorphic targets against which models of subglacial hydrology capable of resolving short timescales as well as the transition between distributed and channelised drainage can be evaluated. In this paper, we used the Glacier Drainage System model (Werder et al., 2013), *GlaDS* hereafter, to explore the basal hydrological conditions associated with murtoo formation beneath the FIS and to evaluate the potential for such models to be used to interrogate palaeo hydrological systems more broadly.

2 Study site

Following the Younger Dryas between 12.7 to 11.7 cal. ka, the eastern margin of the Fennoscandian Ice Sheet (FIS) was located behind the Salpausselkä ice-marginal complexes towards the southern coast of Finland. The mapped distribution of esker systems, interlobate eskers, ice-marginal complexes, streamlined bedforms, and moraines suggests that the continental ice sheet at this time likely consisted of rapidly flowing ice-lobe provinces interspersed with relatively passive interlobate regions (Punkari, 1980; Salonen, 1986; Punkari, 1997; Boulton et al., 2001; Lunkka et al., 2004; Johansson et al., 2005;

https://doi.org/10.5194/egusphere-2023-2141
Preprint. Discussion started: 16 October 2023

Putkinen et al., 2017; Palmu et al., 2021). Ice-lobe provinces characteristically contain a marked concentration of streamlined morpho-lithogenetic units with a coherent orientation (Palmu et al., 2021)—features typically absent from interlobate regions (Ahokangas et al., 2021). Where ice lobes abut adjacent lobes or interlobate regions, the margins are often characterised by large eskers and interlobate glaciofluvial systems, and distally, ice lobes typically terminate in complex ice-marginal assemblages (e.g., the Salpausselkäs) comprising glaciofluvial sandurs and deltas, as well as moraine ridges (Palmu et al., 2021).

Our study site (Figure 1A) is focused on the Finnish Lake District Ice Lobe province described by Putkinen et al. (2017) and Palmu et al. (2021). Encompassing an area of ~57,600 km^2 within southern Finland, the FLDIL consists of a main trunk upstream of a lobate expansion. The lobate portion of the FLDIL is bound at its easternmost margin by the first and second Salpausselkäs (Figure 1A)—large ice marginal complexes, which mark the Younger Dryas extent of the FIS in the region (Donner, 2010; Lunkka et al., 2021). Laterally the main trunk of the FLDIL abuts the NäsijärviJyväskylä ice-lobe to the southwest and the Oulu-North Karelian ice-lobe province to the northeast, as well as both the Päijänne and Middle Ostrobothnian interlobate regions (Putkinen et al., 2017; Palmu et al., 2021). The bedrock within the FLDIL and the wider FIS comprises predominantly crystalline bedrock, dominated by Precambrian schists, gneisses, and granitoids (Lehtinen et al., 2005) with a thin Quaternary overburden (Lunkka et al., 2021). Systematic mapping using LiDAR-derived digital elevation models (e.g., Putkinen et al., 2017) has revealed a high density of drumlims, mega-scale glacial lineations (MSGL), eskers and hummocky moraines in this region (Figure 1C–E). These features are consistently orientated along a principal northwest–southeast axis and, together with the lack of ice-marginal positions postdating the Younger Dryas, suggest there was limited re-organisation of the major ice flow pathways during retreat from the second Salpausselkä margin (Putkinen et al., 2017). The FIS is likely to have collapsed continuously and rapidly following the Younger Dryas (Kleman et al., 1997), retreating northwest towards Norway and gone by 9–10 $\mathrm{cal.\ ka}$ (Hughes et al., 2016; Stroeven et al., 2016; Regnéll et al., 2019). The speed of the retreat, together with the complex landform assemblage suggest that, during deglaciation, the FIS was characterised by high and spatially extensive atmospheric-driven surface melting with limited calving into the Baltic Sea Basin (Greenwood et al., 2017; Patton et al., 2017; Boswell et al., 2019). In this way, the FLDIL, and the FIS more broadly, appear analogous to conditions prevalent in land-terminating portions of the GrIS today (Greenwood et al., 2016; Ojala et al., 2019).

The FLDIL contains a high density of murtoo fields along meltwater routes (Figure 1A Ahokangas et al., 2021). In the FLDIL trunk, murtoos are found amongst ribbed moraines and hummocky moraines (Figure 1C). Collectively, these form longitudinal bands adjacent to the three primary lineation fields containing some of the longest subglacial features in the Lake Lestijärvi area. The clearest association between murtoo routes and eskers is visible in the northeastern longitudinal band (Figure 1D). In the southeastern margin, fewer murtoo routes exist and instead the area is occupied by hummocky routes (Ahokangas et al., 2021). Murtoo routes are most densely concentrated in the central part of the FLDIL trunk, however, within the centre of the lobe numerous water bodies present and a thin sediment cover (Figure A1) may act to mask adjacent areas and contribute to the apparent fragmented arrangement (Ahokangas et al., 2021). As in the trunk, the distribution of murtoo routes within the lobe reflects that of the streamlined terrain (Figure 1E), and the densest pattern of murtoo routes borders or is downstream of the densest arrangement of subglacial lineations in the northern and southern sectors of the trunk. Importantly, few murtoo

https://doi.org/10.5194/egusphere-2023-2141
Preprint. Discussion started: 16 October 2023

fields are found closer than 40 km from the Salpausselkä ice marginal complexes (Mäkinen et al., 2023) at the expected limit of channelised drainage (Chandler et al., 2013; Dow et al., 2015).

3 Methods

To model the basal hydrology of the FLDIL we used the Ice-sheet and Sea-Level System Model (ISSM, Larour et al., 2012, `Revision 27448`) and the implementation of the GlaDS model (Werder et al., 2013) contained therein. We first generated an input ice geometry by depressing a contemporary reanalysis temperature and precipitation dataset to approximate conditions ∼12 cal. ka. Then, using GlaDS parameterised by this input ice geometry and a modified digital elevation model (DEM) of the region, we explored the evolution of basal hydrology in the FLDIL through time. A detailed description is provided below and model parameter values are given in Table 1.

3.1 Model description

The GlaDS model (described in full in Werder et al., 2013) is a 2D finite element model which has been widely applied to contemporary ice sheets in Greenland (e.g., Dow et al., 2018a; Cook et al., 2020, 2022; Ehrenfeucht et al., 2023) and Antarctica (e.g., Dow et al., 2018b, 2020; Indrigo et al., 2021; Dow et al., 2022; McArthur et al., 2023) as well as glaciers in Svalbard (e.g., Scholzen et al., 2021). The GlaDS model includes distributed flow along linked cavities represented by a continuous sheet of variable thickness at mesh elements, and channelised flow through Röthlisberger channels (R-channels) that form along mesh edges of a prescribed unstructured mesh. Water flux, q_s, through the distributed system is driven by the hydraulic potential gradient,$\nabla\emptyset$, along with the sheet conductivity, k_s

$$q_s = -k_s h^{\alpha} |\nabla\emptyset|^{\beta} \nabla\emptyset, \tag{1}$$

where the first (α) and second (β) sheet flow exponents describe fully turbulent flow in the Darcy-Weishbach law, and h is the sheet thickness. Sheet elements exchange water with channels along element edges, the cross sectional area of which S, evolve through time due to the dissipation of potential energy, Π, sensible heat exchange, Ξ, and cavity closure rates due to viscous ice creep v_c

$$\frac{\partial S}{\partial t} = \frac{\Xi - \Pi}{\rho_i L} - v_c, \tag{2}$$

where p_i is the ice density and L is the latent heat of fusion. Channels are able to form along all element edges but only a few will reach a meaningful size (Werder et al., 2013). A key advantage of GlaDS lies in its ability to capture the growth and restriction of these channels entirely due to drainage dynamics, without requiring a predetermined drainage system (Dow et al., 2020). Following Werder et al. (2013), we set a threshold discharge of $Q = 1\,\mathrm{m}^3\,\mathrm{s}^{-1}$ above which an element edge is classified as a channel. Surface melt can either be routed to the bed via a series of moulins, represented as cylinders with a

https://doi.org/10.5194/egusphere-2023-2141
Preprint. Discussion started: 16 October 2023

Table 1. List of input values, values highlighted in bold indicate those used for sensitivity testing and a range of values is provided

Symbol	Description	Default value	Tested range	Units
p_i	ice density	918		$\mathrm{kg\,m^3}$
p_w	water density	1000		$\mathrm{kg\,m^3}$
g	gravitational acceleration	9.81		$\mathrm{m\,s^{-2}}$
n	Glen's flow law exponent	3		
a	basal friction coefficient	0–120		$(\mathrm{Pa\,a^{-1}})^{1/2}$
A	rate factor	1.7×10^{-24}		$\mathrm{s^{-1}\,Pa^{-3}}$
L	latent heat	3.34×10^{5}		$\mathrm{J\,kg^{-1}}$
c_t	pressure melt coefficient	7.5×10^{-8}		$\mathrm{KPa^{-1}}$
c_w	heat capacity of water	4.22×10^{3}		$\mathrm{Jkg^{-1}\,K^{-1}}$
α	first sheet flow exponent	$5/4$		
β	second sheet flow exponent	$3/2$		
α_c	first channel flow exponent	$5/4$		
β_c	second channel flow exponent	$3/2$		
k_s	**sheet conductivity**	10^{-4}	10^{-2}–10^{-5}	$\mathrm{m^{7/4}\,kg^{-1/2}}$
k_c	**channel conductivity**	0.1	0.5–0.05	$\mathrm{m^{3/2}\,kg^{-1/2}}$
E_{vr}	**englacial void ratio**	10^{-4}	10^{-3}–10^{-5}	
l_c	sheet width below channel	2		m
A_m	moulin cross-sectional area	10		$\mathrm{m^2}$
l_r	cavity spacing	2		m
h_r	**basal bump height**	0.085	0.05–0.1	m
b_{melt}	**basal melt rate**	5×10^{-3}	1–7×10^{-3}	$\mathrm{m\,yr^{-1}}$
U_b	**mean annual velocity**†	150	100–200	$\mathrm{m\,yr^{-1}}$
$N_{moulins}$	**number of moulins***	2500	1000–4000	

† We tested both a transient and temporally constant velocity within these given ranges for mean annual velocity

* We also ran an experiment in which melt was routed directly to the bed at each node (SHEET)

https://doi.org/10.5194/egusphere-2023-2141
Preprint. Discussion started: 16 October 2023

fixed cross sectional area, $A_m = 10\,\mathrm{m}^2$, or delivered directly to the bed at every node. Finally, an englacial void ratio term, e_v controls the volume of water stored in englacial aquifers to mimic the observed delay between daily maximal melt input and peak proglacial discharge (Werder et al., 2013).

3.1.1 Boundary conditions and forcings

To model basal hydrology, GlaDS requires user inputs for bed elevation, z_b and ice thickness, h as well as boundary conditions and parameters (Table 1) detailed below. We anticipate that the modern surface elevation is not representative of that $\sim$12 cal. ka. As the baseline boundary condition, z_b, we account for changes, particularly in terrain associated with the Salpausselkä ice marginal formation, by subtracting Quaternary sediment thickness estimates (GTK, Finland, 2010) from the 25 m/pixel EU-Digital Elevation Model V1.1 (available at: https://www.eea.europa.eu/data-and-maps/data/copernicus-land-monitoring-service-eu-dem). Because lake bathymetry was only partially available we did not subtract this from our input DEM in the baseline model. We also did not adjust our model to account for differences in elevation due to glacial isostatic adjustment (GIA) since $\sim$12 cal. ka. Available sea-level markers from Rosentau et al. (2021) and Ojala et al. (2013) suggest that uplift of $\sim$80 m has occurred in the southeastern portion of our domain, and up to 200 m in the northwest since $\sim$12 cal. ka. Combined with eustatic sea level rise, these differences account for a maximum of 100 m difference in elevation and a tilting of the basin towards the southeast during glaciation, which varied through time. To ensure the stability of GlaDS the input DEM was smoothed using a low-pass filter. Finally, within steep terrain, an anisotropic mesh ($n_{nodes} \approx 19,000$) was refined based on z_b such that element edges were shortest (to a minimum edge length of 400 m) in rougher terrain and longer where terrain was flatter (to a maximum edge length of 2 km). As boundary conditions, we imposed a zero flux condition on the domain edge everywhere expect at the ice terminus, where given spatial uncertainty around water depth, an outlet Dirichlet condition equivalent to atmospheric pressure was prescribed. By enforcing zero input flux we neglect to include water input from beyond the model domain and we also do not account for any exchange of water between adjacent ice lobe provinces. To promote model stability, we used an adaptive timestep that was allowed to vary between one hour and $\sim$90 seconds and all of our transient models were run for 10,000 days, or $\sim$27 years.

An approximation for the FIS ice thickness, h, at $\sim$12 cal. ka within the FLDIL was generated using the 2D Shallow-Shelf Approximation (SSA, MacAyeal, 1989) within ISSM (Larour et al., 2012). Ice is assumed to be isothermal with a viscosity, B, equivalent to an ice temperature of -5 °C (from Cuffey and Paterson, 2010, p.73; rate factor, A, listed in Table 1). In reality, ice temperature is both spatially and temporally variable, however, without using a more detailed thermomechanical ice model here, we follow the previous ad-hoc assumptions of Nick et al. (2013) for the GrIS and Åkesson et al. (2018) for the FIS, by setting our ice temperature to -5°C. Basal motion was modelled using a viscous sliding law (Budd et al., 1979) and following Åkesson et al. (2018) we used a spatially variable basal drag coefficient, α, proportional to bed z_b, given by:

$$\alpha = 120 \frac{\min\left(\max\left(0, z_b + 800\right), 2000\right)}{2000}. \tag{3}$$

https://doi.org/10.5194/egusphere-2023-2141
Preprint. Discussion started: 16 October 2023

To reach volumetric steady state, defined for our ice sheet model as differences in ice volume between successive iterations of less than $10^{-6}\,\mathrm{km}^3$, we ran the ice sheet model for 20,000 years with a adaptive timestep, allowed to vary between 1 day and 1 year. An initial estimate of ice surface elevation was given using a parabolic profile as a function of distance from the terminus, and initialisation values for velocity were calculated using a stress balance solution for this ice surface. Dirichlet conditions were imposed at the mesh edges along the boundary with zero inflow.

We used climatic forcing both for our ice sheet model and for GlaDS. The $12\,\mathrm{cal.\,ka}$ climate was estimated using a modern (1981-2010) reanalysis dataset (see Abatzoglou et al., 2018). Precipitation was kept at the contemporary monthly value, but we depressed monthly temperature by $15^{\circ}\mathrm{C}$, approximately the temperature differential indicated by NGRIP $\delta 18\mathrm{O}$ records (Johnsen et al., 1997). To calculate surface mass balance efficiently in our long term ice sheet model we used a simple positive degree day (PDD) model (as in Cuzzone et al., 2019) allowed to vary about a fixed Gaussian distribution with standard deviation, $\sigma_{PDD} = 5.5^{\circ}\,\mathrm{C}$ around the monthly mean and a lapse rate of $7.5^{\circ}\mathrm{C\,km}^{-1}$. However, our focus here is on the basal hydrology and we used a modified PDD scheme to estimate meltwater production for our GlaDS simulations.

It is commonly assumed that the total monthly positive degree days can be represented by a fixed Gaussian distribution with $\sigma_{PDD} \approx 5.5^{\circ}\,\mathrm{C}$ (e.g., Braithwaite and Olesen, 1989). However, field measurements suggest that this does not hold for the GrIS (Wake and Marshall, 2015), particularly at temperatures $\geq -5^{\circ}\,\mathrm{C}$. Instead, Wake and Marshall (2015) suggest monthly variability in temperature, σ_M, is more accurately described by a quadratic function:

$$\sigma_M = -0.0042T_M^2 - 0.3T_M + 2.64, \tag{4}$$

where T_M is the mean monthly temperature. This function accounts for the observation that variability in temperature decreases with increasing temperatures (Gardner et al., 2009; Marshall and Sharp, 2009; Fausto et al., 2011) due to heat buffering, which promotes a more stable boundary layer (Wake and Marshall, 2015). We used the calculated σ_M to add Gaussian noise to a daily temperature record estimated by linearly interpolating our depressed MAT record. The number of positive degree days per month, PDD_M was taken as $PDD_M \geq -5^{\circ}\,\mathrm{C}$. We used $-5^{\circ}\,\mathrm{C}$ as our threshold (rather than the more commonly used $0^{\circ}\,\mathrm{C}$ threshold) to account for melt which may occur even for days with an average temperature of $0^{\circ}\,\mathrm{C}$ (see van den Broeke et al., 2010). Finally, we used melt rate factors $\gamma_{ice} = 17.22\,\mathrm{mm\,per\,PDD}$ and $\gamma_{snow} = 2.65\,\mathrm{mm\,per\,PDD}$ following Cuzzone et al. (2019) keeping these consistent between our ice sheet model and GlaDS model. Monthly melt was kept fixed annually for each run. Melt varied in absolute terms between individual simulations but the mean melt and standard distribution remained identical throughout.

Total monthly melt was then converted to yearly melt rates and routed to the bed via a series of moulins. Without detailed surface topography and following Werder et al. (2013) we divided our domain using Voronoi tessellation around on a randomly distributed series of points. Within each Voronoi cell, acting as a 'catchment zone', the lowest elevation node was identified and used as the location for a moulin towards which all other nodes flow. Surface melt rate was integrated over each catchment and converted to instantaneous moulin discharge, Q_m^k.

https://doi.org/10.5194/egusphere-2023-2141
Preprint. Discussion started: 16 October 2023

3.1.2 Steady state and sensitivity testing

To avoid overwhelming our initial system with sudden meltwater inputs and to approximate a wintertime hydrology configuration, we first ran GlaDS to steady state with no surface melt and fixed basal meltwater input. Informed by sensitivity testing and previous work (e.g., Werder et al., 2013; Dow et al., 2018b, 2020; Indrigo et al., 2021), the values listed in Table 1 were used as input parameters to GlaDS. To ensure the majority of nodes pressured at the end of our steady state run, we used a fixed velocity of $30\,\mathrm{m a^{-1}}$. Given uncertainty regarding the spatial variability of basal melt rates, which vary as a function of geothermal heat and frictional heating, we used a spatially and temporally constant basal water input (as in Dow et al., 2018a, c, 2020; Poinar et al., 2019). Basal melt rates beneath the GrIS typically range between 1–$7\times10^{-3}\,\mathrm{m\,yr^{-1}}$ (see Karlsson et al., 2021) and we used $5\times10^{-3}\,\mathrm{m\,yr^{-1}}$ for our steady state configuration and the majority of the subsequent transient runs. To test the influence of basal melt rates on our system we ran an additional low basal melt rate ($1\times10^{-3}\,\mathrm{m\,yr^{-1}}$) and high basal melt rate scenario ($7\times10^{-3}\,\mathrm{m\,yr^{-1}}$) to steady state. Here, steady state was reached once the median difference in water depth between two successive steps was less than $10^{-6}\,\mathrm{m}$. All three basal melt scenarios reached this by 20,000 days, and nodes reached ~90% of overburden pressure [1] with no channel formation.

For the default transient model run, we used the end member configuration of our steady state run as an initialisation state with the addition of transient surface melt routed to the bed via ~2500 moulins, a density of 0.04 moulins per $\mathrm{km^2}$. Measured moulin density varies between 0.02 to 0.09 moulins per $\mathrm{km^2}$ in Greenland (Yang and Smith, 2016). To test the sensitivity of our system to moulin density we also ran models with ~1000 (0.02 per $\mathrm{km^2}$), ~4000 (0.06 per $\mathrm{km^2}$), and two further randomly generated configurations of the default ~2500 (0.04 per $\mathrm{km^2}$). We also tested an additional configuration in which melt at every node was routed directly to the bed. Further sensitivity testing was carried out for several poorly constrained parameters in GlaDS (listed in bold in Table 1), as well as for the basal geometry and moulin density. The conductivity of both the sheet, k_s and channels, k_c are the key controls on the extent and spacing of channels, with the basal bump height, h_r, and basal velocity also important. For basal velocity, we tested both a temporally fixed and temporally variable velocity, with the transient velocity varying between 85% and 140% of the mean to approximate speed-ups at the onset of the melt season and winter slowdowns commonly observed in Greenland (e.g., Sole et al., 2013). Without a more detailed understanding of past dynamics, velocity was kept spatially uniform throughout. Although the default configuration describes a terrestrial margin, we also tested the influence of a shallow body of water at the ice margin by prescribing Dirichlet conditions at the ice margin where pressure is equivalent to that of a uniform 30 m water depth. To explore the influence of our modified topography boundary condition, we ran tests with a uniformly flat bed, one representing contemporary terrain (without Quaternary sediment thickness removed), and one with the available partial lake bathymetry removed. Finally, we also explored the dependency of our results on mesh geometry, including using a coarser mesh (maximum edge length of 5 km), a mesh not refined by elevation in any way, and a mesh in which a coarse mesh (edge length between 5–8 km) was prescribed >80 km from the ice margin and a much finer mesh (edge length ≈300 m) was prescribed <80 km from the ice margin.

[1] Borehole measurements of overwinter pressure in the distributed drainage system have been measured at 80-90% of overburden pressure (e.g., Harper et al., 2021)

https://doi.org/10.5194/egusphere-2023-2141
Preprint. Discussion started: 16 October 2023

3.2 Model validation from geomorphological datasets

Finally, we compared the GlaDS output to geomorphological evidence. We first masked model nodes falling within 40–60 km of the ice margin within the hypothesised range of murtoo formation (e.g., Ojala et al., 2019). We then queried these nodes according to whether they occurred within a mapped meltwater route; sub-dividing these routes based on the presence or absence of murtoo fields. Using 500 m buffers, we approximated the lateral extent of meltwater routes along 2D polylines representing their central long-axis from Ahokangas et al. (2021). In total, 1205 nodes occur in murtoo hosting meltwater routes, 951 nodes in murtoo *free* meltwater routes, and 244 nodes that are not associated with any meltwater routes but are between 40–60 km of the ice margin. Visual comparison was also made to esker deposits within the FLDIL mapped by Palmu et al. (2021).

4 Results

In total, 30 simulations were run, all of which successfully converged. In Section 4.1 we discuss our baseline test, and in Section 4.2 we report the parameter and forcing dependencies. For each model run, we examined the subglacial water pressure, expressed as a percentage of the overburden pressure (overburden$_{\%}$, sheet discharge, q_s on element faces; channel discharge Q_c on element edges (where $Q \geq 1\mathrm{m}^3\,\mathrm{s}^{-1}$) and water velocity.

4.1 Baseline scenario

After an initial adjustment from steady state to transient forcing over 10 years, the baseline model reached a quasi-steady state configuration in which the system responded seasonally to summer meltwater input (Figure A2). Figure 2 shows the median summer and winter state of the baseline run in terms of pressure expressed as a percentage of overburden, overburden$_{\%}$ (Figure 2A), discharge within sheet elements, q_s (Figure 2B), water velocity, V_W (Figure 2C), and channel discharge, Q_s (Figure 2D) as well as mapped murtoo fields from Ahokangas et al. (2021). In summer, channels, shown as black solid lines (Figure 2A–C) typically extend up to 40 km from the ice margin creating valleys of low overburden$_{\%}$ (Figure 3A). Between 40 km and up to 60-70 km from the ice margin, in the transitional area between inefficient and efficient modes of drainage, overburden$_{\%}$ approaches and exceeds 100% of overburden. Beyond 70 km from the ice margin, with zero channelisation and widespread inefficient drainage, overburden$_{\%}$ is uniformly at $\sim 80\%$. Towards the ice margin, q_s sharply increases 60 km from the margin in both summer and winter (Figure 2B). In summer, as channels draw down water from surrounding areas, q_s approaches $10^{-1}\,\mathrm{m}^3\,\mathrm{s}^{-1}$ between channels. In winter, with limited channel discharge, the highest sheet discharge is found within 40–60 km of the ice margin ($\sim 1\times10^{-3}\mathrm{m}^3\,\mathrm{s}^{-1}$ Figure 2B). Throughout the year, V_W remains high ($\sim 1.5\times10^{-3}\mathrm{m\,s}^{-1}$) at the ice margin. During summer, V_W in the sheet reflects the concentration of drainage into channelised systems 0–40 km from the ice margin, with velocities $\sim 8\times10^{-4}\mathrm{m\,s}^{-1}$ persisting up to 50 km from the ice margin. In winter, the drop in velocity away from the ice margin is sharper, and higher water velocities ($> 5\times10^{-4}\mathrm{m\,s}^{-1}$) are limited to less than 50 km from the margin. Finally, Figure 2D shows Q_c with $\sim$ 35 parallel–sub-parallel channels visible in summer, during which

https://doi.org/10.5194/egusphere-2023-2141
Preprint. Discussion started: 16 October 2023

median discharge reaching a maximum of $100\,\mathrm{m^3\,s{-}1}$. A number of channels have an anabranching structure as well as small tributaries. In winter, a number of channels persist with a maximum median discharge of $3\,\mathrm{m^3\,s{-}1}$ (Figure 2D).

Figure 3C shows the system state during September of model year 19, arbitrarily chosen as a representative example of the model state at the end of a melt season. As in Figure 2, a sub-parallel pattern of channels emerges in summer months (Figure 3C), with channels arranged perpendicular to, and extending up to $\sim 50\,\mathrm{km}$ inland of, the ice margin. Approximately 40 main channels are evident in late summer (Figure 3), evenly spaced every $\sim 5\,\mathrm{km}$ laterally, each of which is also fed by one to two levels of anabranching lower-order tributaries. Following the initial period of adjustment to transient forcing, peak discharge for these channels is $200\,\mathrm{m^3\,s{-}1}$ during summer (~June) each year with a maximum cross-sectional channel area of $42\,\mathrm{m^2}$ (equivalent to a half-circle with radius, $r \approx 5\,\mathrm{m}$). Many channels exhibit a biannual pattern of growth and decay (e.g., Figure 3B) persisting throughout the winter between two consecutive summers. Following initial channel growth after the onset of the melt season (preceded by a sharp increase in overburden pressure), Q_c of these persistent channels trends towards $1\,\mathrm{m^3\,s{-}1}$ but does not fall below the channelisation threshold before the following summer. As a result, subsequent meltwater input through these persistent channels is quickly accommodated with only a small increase in $\mathrm{overburden}_{\%}$ (Figure 3B). An alternating spatial pattern of overwinter persistence is evident. Channels in the centre of the FLDIL lobe persist through winters in which no channels persist nearer to the lateral margins, and vice versa the following winter, with no overwinter channels evident during winters in which lateral margin channels persist overwinter (Movie A1).

In the ice interior, at the head of modelled channels, a persistent area of low effective pressure (where the overburden percentage, $\mathrm{overburden}_{\%}$ approaches and exceeds 100%) develops each melt season (Figure 2A) following the onset and migration up-glacier of surface meltwater inputs. Figure 3D–E demonstrates the seasonal evolution of two nodes in this area, each associated with channel systems. Each node undergoes a rapid seasonal increase in overburden pressure to $\lessapprox 120$ % with a more gradual decrease thereafter. At node 3,842 (Figure 3E) this pattern repeats annually—every year the decrease in overburden following an initial increase is accompanied by peaks in q_s, Q_c, and V_W and the development of channels throughout the meltwater season. However, a more complex biannual signal is evident at node 16,402 (Figure 3D), which is located $\sim 0.7\,\mathrm{km}$ from a murtoo field. Each year, there is a sharp increase in $\mathrm{overburden}_{\%}$ at the start of the melt season, however, the subsequent drop in overburden varies every other year. Either the overburden spikes and then drops rapidly over 1-2 months to the winter value (~80%) until the following melt season, or the drop in overburden is initially shallower before quickly dropping to an elevated pressure (~90%) relative to the previous winter. Years in which the drop in overburden is more gradual are also associated with low values of Q_c and higher q_s. In contrast, years that have a rapid drop in overburden pressure after the melt season are associated with larger channels, with Q_c approaching $10^0\,\mathrm{m^3\,s{-}1}$. Beyond $100\,\mathrm{km}$, upglacier of any significant surface melt inputs to the bed, only limited seasonal evolution of the hydrological system is evident (e.g., Figure 3A). Here, the system is effectively inert, remaining at $\rho_O \approx 80\%$ with only small periodic perturbations in q_s, Q_c, and V_W.

Focusing on nodes 40–60 km from the ice margin, within the distance thought to be associated with murtoo formation at this time period (Ojala et al., 2019), we grouped nodes according to whether they fall i) within the boundary of a mapped meltwater route and that route also hosts a murtoo field, ii) within the boundary of a mapped meltwater routes that *does not* contain a

https://doi.org/10.5194/egusphere-2023-2141
Preprint. Discussion started: 16 October 2023

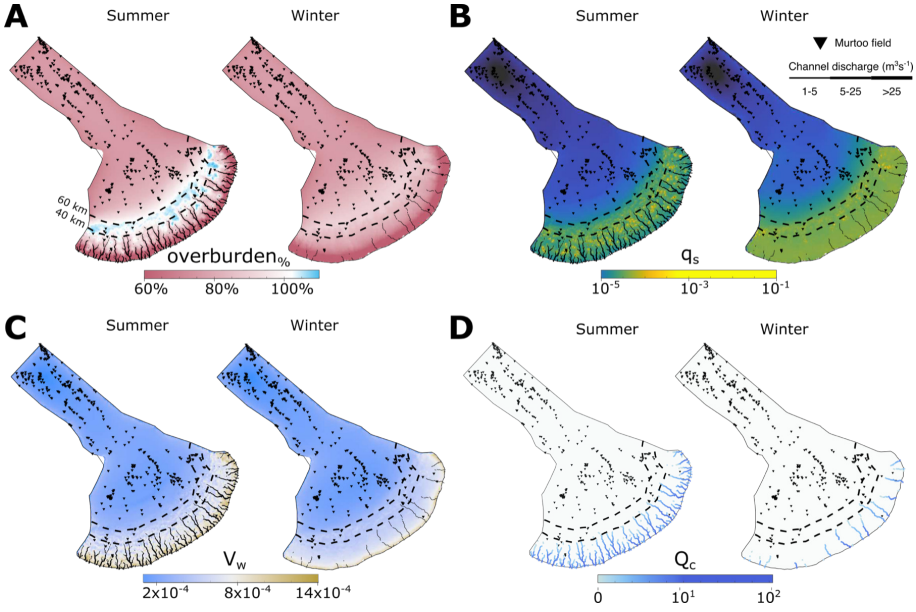

Figure 2. Median summer and winter system states in the baseline model run. **A**) Water pressure expressed as a percentage of overburden pressure, overburden$_{\%}$. In summer and winter, channels, shown as black solid lines (here and in panels B & C) **B**) Sheet discharge, q_s. **C**) Water velocity, V_W. **D**) Channel discharge, Q_c. For each output, we took the median from model years 5–27 disregarding the initial period of adjustment to transient forcing. *Summer* extends from May to September, all other points fall into *winter*. Note that the scales for panels B and D are logarithmic. Dashed lines in all panels indicate contours of 40 and 60 km from the ice margin.

murtoo field, and iii) beyond any mapped meltwater routes (all other nodes)(Figures 4 & 5). Nodes that fall within a meltwater route (Groups i, $n = 955$ & ii, $n = 244$) show strong seasonal variation and throughout the year have higher overburden$_{\%}$, q_s, V_W, and Q_c than nodes that do not fall within a mapped meltwater route. The median signal of nodes within meltwater routes is one of sharp increases at or just following the onset of the melt season, followed by a more gradual decline into winter (Figure 4). One-way ANOVA analysis in which the values of overburden$_{\%}$, q_s, V_W, and Q_c between groups i–iii were considered without respect to time, indicates that there is a statistically significant difference in the population marginal means (or the mean within each grouping) of the three categories ($p < 0.05$ at the 95% confidence interval).

Additionally, we grouped each node observation within calendar months (Figure A32). Comparison of groups i–iii within each month—using two-way ANOVA analysis and the Tukey-Kramer HSD Test for multiple comparisons of unequal group sizes—indicate that there are significant differences ($p < 0.05$) between the population marginal means throughout the year (Tables A1–A4). In terms of overburden$_{\%}$, both groups of meltwater routes are significantly higher than nodes outside of meltwater routes during every month. However, both meltwater route groups are also significantly different from each other every month. Between January and April, overburden$_{\%}$ is significantly higher in murtoo-hosting meltwater routes nodes than in murtoo-free meltwater routes. Following the onset of the melt season, during June and July, overburden$_{\%}$ is lower in group i nodes than in group ii nodes, before again returning to higher overburden$_{\%}$ in group i nodes relative to group ii nodes between

https://doi.org/10.5194/egusphere-2023-2141
Preprint. Discussion started: 16 October 2023

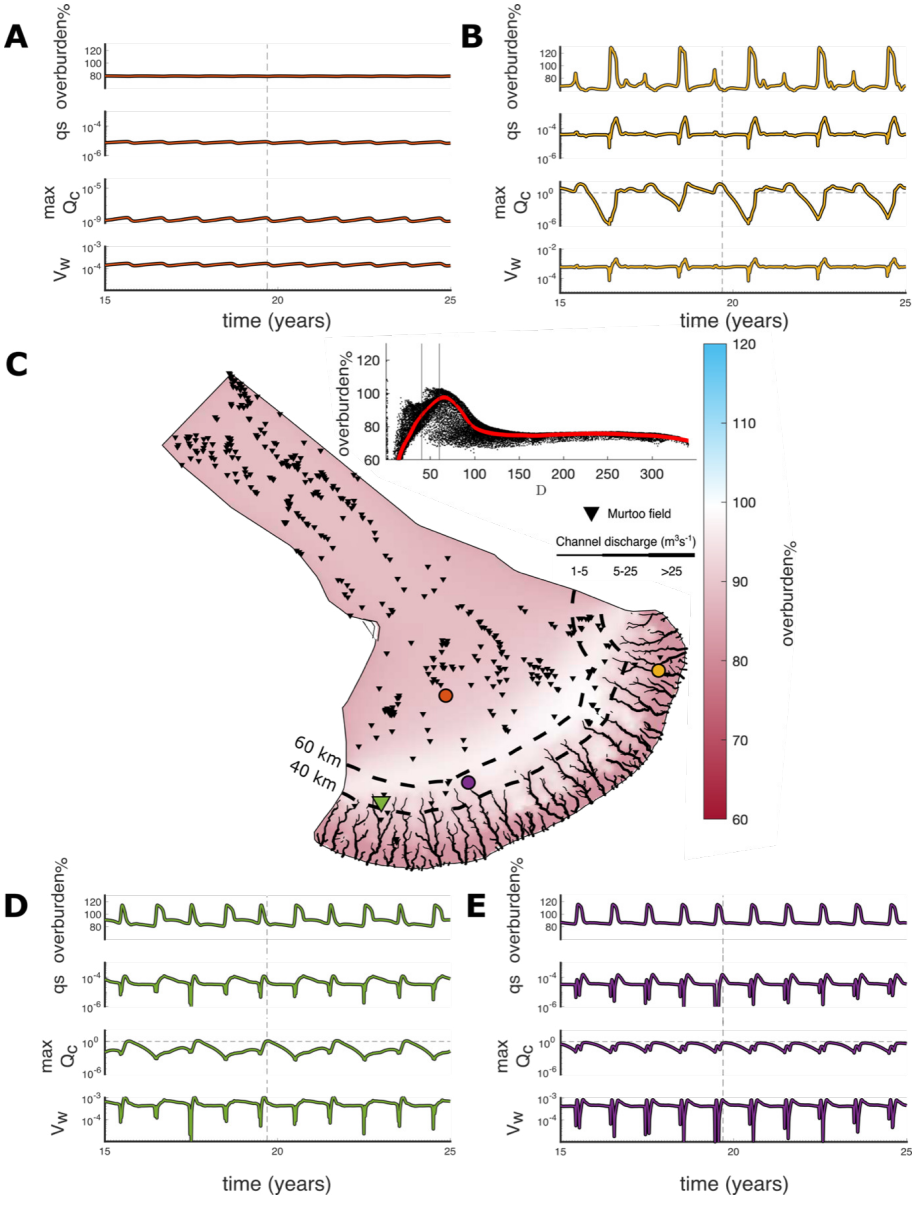

Figure 3. The evolution of overburden (overburden$_{\%}$), sheet discharge (q_s), water velocity (V_W), and channel discharge (Q_c) at four nodes during an arbitrarily chosen span over model years 15–25. **A**) Node No. 6,277 located ∼120 km from the ice margin. **B**) Node No. 18,517 located ∼17 km from the ice margin. **C**) Overburden at the end of the melt season in model year 19. Channels are represented as black lines, murtoo fields as inverted black triangles, and the location of panels A, B, D, and E as coloured points. Inset shows overburden at every node as a function of distance, D from the ice margin with a smoothing function shown in red and vertical lines at 40 and 60 km from the ice margin. **D**) Node No. 16,402 located 0.7 km from a murtoo field and ∼45 km from the ice margin. **E**) Node No. 3,842 located ∼54 km from the ice margin at the head of a channel system without an adjacent murtoo field. The time slice shown in panel C is represented as a vertical dashed line in panels A, B, D, and E. Note the logarithmic scale for q_c and Q_c.

https://doi.org/10.5194/egusphere-2023-2141
Preprint. Discussion started: 16 October 2023

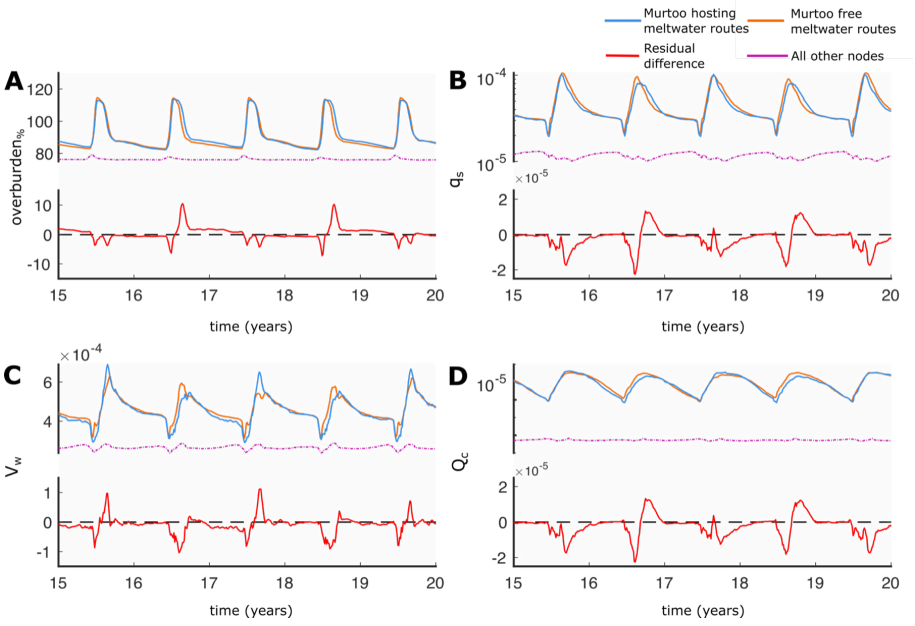

Figure 4. Median output during model years 15–20 at nodes between 40–60 km from the ice margin. In all panels, nodes which fall within mapped meltwater routes that do not contain murtoo fields (murtoo hosting) are shown in orange, those that fall within meltwater routes which do host murtoos (murtoo free) are shown in blue, and all other nodes are shown in dashed purple. The red line in each panel represents the residual difference between the median of murtoo hosting meltwater routes and murtoo free meltwater routes. A positive residual indicates higher median values in murtoo hosting meltwater routes, and vice versa for negative residual values. **A**) Water pressure expressed as a percentage of overburden, overburden$_{\%}$ **B**) Sheet discharge, q_s. **C**) Water velocity, V_W. **D**) Channel discharge, Q_c. Note panels B and D have logarithmic scales.

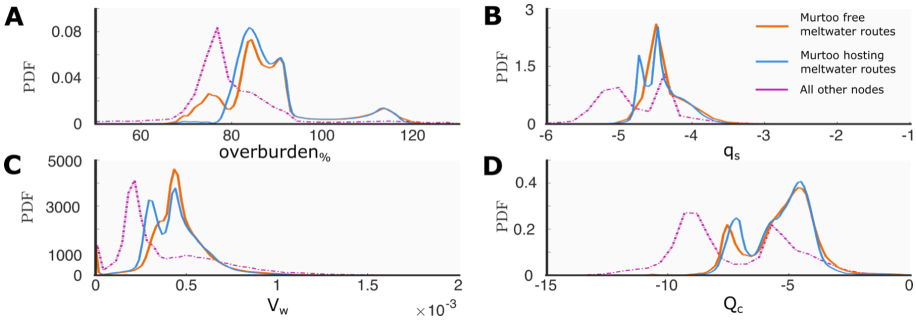

Figure 5. Probability density estimates from kernel smoothing of output parameters during all model years at nodes between 40–60 km from the ice margin. As in Figure 4, nodes which fall within mapped meltwater routes that do not contain murtoo fields (Murtoo hosting) are shown in orange, those that fall within meltwater routes which do host murtoos (Murtoo free) are shown in blue, and all other nodes are shown in dashed purple. **A**) Water pressure expressed as a percentage of overburden, overburden$_{\%}$ **B**) Sheet discharge, q_s. **C**) Water velocity, V_W. **D**) Channel discharge, Q_c. Note panels B and D have logarithmic scales.

https://doi.org/10.5194/egusphere-2023-2141
Preprint. Discussion started: 16 October 2023

August–December. In terms of q_s (Table A2) both groups of meltwater routes are higher than nodes beyond meltwater routes all year. Between January and May there are no significant differences between murtoo hosting, and murtoo free, meltwater routes. However, between June and December, q_s is significantly lower in murtoo hosting meltwater routes than in murtoo free meltwater routes. There is no significant difference between any group in terms of Q_c with the exception of between June–October (Table A3), when Q_c is significantly higher outside meltwater routes. Finally, throughout the year, V_W is higher in mapped meltwater routes than beyond them (Table A4). In murtoo hosting meltwater routes V_W is significantly lower for each month than in murtoo free meltwater routes.

4.2 Sensitivity tests

The parameter sensitivity of basal drainage within GlaDS has already been extensively explored by Werder et al. (2013) and as such we do not conduct a detailed review here. However, in order to best apply the model to a palaeoglacial setting, we did explore the relevant parameter space throughout the ranges indicated in Table 1 and describe the outcome of these changes below. In GlaDS, the spacing and lengths of channels, and in turn the influence of these channels on water pressure at the channel limits, is most sensitive to k_s and k_c, describing the sheet and channel conductivity respectively. At the highest sheet conductivity ($k_s = 10^{-2}\,\mathrm{m}^{7/4}\,\mathrm{kg}^{-1/2}$, Figure A3) no channels longer than one km are formed and water pressure is efficiently evacuated at relatively low pressures (<60% of overburden). With a lower sheet conductivity ($k_s = 10^{-3}\,\mathrm{m}^{7/4}\,\mathrm{kg}^{-1/2}$, Figure A4), around 60 channels were largely limited to within $\sim 10\,\mathrm{km}$ of the ice margin, and an area of low effective pressure 40–60 km of the ice margin was limited to a short one month period at the peak of the melt season. At a minimum sheet conductivity of ($Kk_s = 10^{-5}\,\mathrm{m}^{7/4}\,\mathrm{kg}^{-1/2}$, Figure A5) ∼40 channels extend up to 50 km back from the ice margin. These channels appear more complex than those in the baseline run, with a more sinuous geometry and higher number of tributaries. Additionally, an extended area of low (but not zero) effective pressure extends up to 150 km from the ice margin.

At the maximum channel conductivity ($K_C = 0.5\,\mathrm{m}^{3/2}\,\mathrm{kg}^{-1/2}$, Figure A6), ∼30 relatively linear channels extend up to 60 km from the ice margin. The area of low-pressure is similarly pushed back to between 60–80 km from the ice margin, and these pressures remain consistently below ~ 90 % of overburden. At $k_c = 0.05\,\mathrm{m}^{7/4}\,\mathrm{kg}^{-1/2}$ (Figure A7 ~ 30 channels are limited to ∼40 km of the ice margin. Within the 40–60 km distance from the ice margin, water pressures are consistently in excess of 100% of overburden throughout summer. At the lowest value of channel conductivity tested here ($k_c = 10^{-3}\,\mathrm{m}^{7/4}\,\mathrm{kg}^{-1/2}$, Figure A8) a number of high pressure channels are restricted to within 1 km of the ice boundary, with a zone of high water pressure (>100% of overburden) extending 70 km from the ice margin.

Changing the moulin density also alters the density, length, and complexity of channels as well as pressure beyond the upper limit of channel length. At the minimum moulin density tested ($N_{moulins} = 1000$, Figure A9), approximately 25 channels extend up to 50 km from the ice margin, the location of which closely follow the position of high discharge moulins near to the glacier terminus. A consequence of this is that high water pressure is less spatially continuous 40–60 km from the ice margin, though still in strong agreement with murtoo field location. A higher moulin density ($N_{moulins} = 4000$, Figure A10) with lower discharge has a similar impact on the spatial distribution of channels as increasing the conductivity of the sheet, with ∼60 channels reaching a maximum of 10–20 km from the ice margin, the location of which appears limited to the lowest

https://doi.org/10.5194/egusphere-2023-2141
Preprint. Discussion started: 16 October 2023

elevation moulins closest to the margin at which higher discharges are prescribed. With lower discharge moulins also existing upglacier however, an area of high water pressure extends up to 70 km from the ice margin. Routing water directly to the bed at every node instead of concentrating discharge through moulins (Figure A11) increases the frequency of short channels ($\sim$5 km) but does not alter the spacing of larger channels, which extend up to $\sim$40 km from the ice margin. Without water input at specific moulins, the area of low pressure associated with larger channels does extend further, with a clear pressure influence extending a further 10 km beyond each channel head. Two different random variations of the default moulin density (Figures A12 & A13) altered the exact location of channels and pressure around these channels, but did not alter the overall pattern of pressure or drainage.

Changing the basal melt rate between 1–7$\times 10^{-3}$ m yr^{-1} (Figures A14 & A15) had little impact on the pattern of channelisation and on pressure 40–60 km of the ice margin, likewise neither did altering the basal bump height between 0.1–0.05 m (Figures A16 & A17). Changing the mesh characteristics by not refining the mesh with respect to elevation alters the absolute position and detailed expression of channels but does not alter their spacing, length, or drainage in terms of pressure and discharge (Figure A18). Using a coarser mesh (Figure A19) lengthens channels, but this likely reflects the accompanying change in catchment areas and resultant drainage patterns through fewer moulins. Increasing the resolution within 80 km of the ice margin (Figure A20, results in major channels (those with a length longer than 20 km) extending up to 5 km further, but with a lower discharge over their full length, supplemented by more frequent small channels within 10 km of the margin. The absolute position of large channels changes compared to the default mesh, but their horizontal spacing remains consistent.

Modelling with a flat bed (Figure A21), using a modern bed (without removing Quaternary sediment thickness, Figure A22), and including the available lake bathymetry has limited impact on channel density, length or drainage (Figure A23). Changing the terminus boundary conditions to approximate drainage into a shallow ($\sim$30 m deep) water body (Figure A24) also has limited influence on our results. Raising the englacial void ratio ($E_{vr} = 10^{-3}$, Figure A25) results in more complex channel geometry, and by increasing storage englaically, confines pressure variability nearer to channels. Lowering the englacial void ratio ($E_{vr} = 10^{-5}$, Figure A26) has no clear influence on channel geometry or pressure.

Finally, changing the basal ice velocity to a fixed value of 100 m yr-1 (Figure A27) lowers the water pressure 40–60 km from the ice margin by $\sim$10% but does not alter channel spacing or length, while raising the basal ice velocity to a fixed value of 200 m yr-1 (Figure A28) lowers the water pressure of channels $<$40 km from the ice margin. Introducing annual transient variability in velocity with a mean velocity of 150 m yr-1 (Figure A29) limits the maximum length channels attain to $\sim$40 km from the ice margin relative to a fixed velocity and more tightly constrains the observed summer water pressure equal or exceeding overburden to within 40–60 km from the ice margin. A transient velocity with a mean of 100 m yr-1(Figure A30) does not clearly impact channels or pressure $<$60 km from the ice margin but does lower the water pressure further from the ice margin by $\sim$5%. A transient velocity with a mean of 200 m yr-1 (Figure A31) has the opposite influence on water pressure $>$60 km from the ice margin.

https://doi.org/10.5194/egusphere-2023-2141
Preprint. Discussion started: 16 October 2023

5 Discussion

5.1 Seasonal drainage in a palaeoglacial setting

The potential for comparing records of palaeo basal hydrology to subglacial hydrology model was recently demonstrated by Kirkham et al. (2022) evaluating hypotheses of tunnel valley formation using an upstream area routing algorithm (Arnold, 2010), a sediment erosion rate model (Carter et al., 2017), and modelled reconstructions of the British and Irish Ice Sheet (Clark et al., 2021). By comparison against seismic profiles of tunnel valleys in the North Sea, Kirkham et al. (2022) found their formation to be most consistent with seasonal fluxes of meltwater delivered to the bed, and not single event outburst floods as previously hypothesised (see Hooke and Jennings, 2006). However, because tunnel valleys and eskers likely represent episodic drainage over millennial timescales during ice sheet retreat (Clark and Walder, 1994; Mäkinen, 2003) the area routing algorithm used by (Kirkham et al., 2022), and similar algorithms used by other studies (e.g., Livingstone et al., 2013a, b, 2015; Karlsson and Dahl-Jensen, 2015; Shackleton et al., 2018), make several simplifying assumptions about the pressure at which water exists, typically assuming water is at or near overburden pressure everywhere. While this assumption greatly reduces the computational expense of modelling subglacial water flow, and has been shown to be a realistic representation of average pressure over an entire melt-season in Greenland (e.g., Banwell et al., 2013), it neglects dynamics associated with conditions variable over seasonal–diurnal timescales. Further, such area-routing algorithms are inherently channelised and do not capture any transition between drainage modes (Banwell et al., 2013).

In contrast to previously examined landforms such as eskers and tunnel valleys, murtoos are thought to form within a transitional drainage regime as widespread distributed systems give way to efficient and channelised drainage (Ojala et al., 2019). In this way, their predicted genesis allow us to constrain and define a parameter space for basal hydrology models such as GlaDS. The weak to moderate deformation of murtoo sediments periodically evident within murtoo vertical exposures indicates that water pressure remained at or close to overburden for sustained periods of time during murtoo formation (Becher and Johnson, 2021; Mäkinen et al., 2023; Hovikoski et al., 2023). The broad and low geomorphology of murtoos, together with internal horizons that are vertically arcuate along a comparable path to the surface, suggest that murtoo deposition occurred within a low and broad cavity reaching a maximum water depth of 1 m (Hovikoski et al., 2023; Mäkinen et al., 2023). As discharge increases through a melt season, the cavity enlarges and is able to accommodate more sediment and water flow before closing as water discharge decreases late in the melt season (Becher and Johnson, 2021; Mäkinen et al., 2023; Hovikoski et al., 2023). Crucially, the cavity never enlarges enough to form a channel of any appreciable size (Mäkinen et al., 2023). Instead murtoo formation is suggested to occur 40–60 km from the ice margin where modelling of the basal hydrology in Greenland indicates shallow surface gradients limit the water supply necessary to grow low pressure channels (Dow et al., 2015). These low ice surface gradients together with surface melt input instead permits only limited broad canals within a pressurised *semi*-efficient drainage system (e.g., Bartholomew et al., 2011; Chandler et al., 2013; Greenwood et al., 2016; Ojala et al., 2019; Hooke and Fastook, 2007; Becher and Johnson, 2021; Mäkinen et al., 2023).

In our base model and many of the sensitivity tests, at the edge of channelised drainage 40–60 km from the ice margin, GlaDS closely matches several predictions for murtoo genesis and their depositional environment. Across the full model do-

https://doi.org/10.5194/egusphere-2023-2141
Preprint. Discussion started: 16 October 2023

main <70 km upglacier from the ice margin, the system exhibits a periodic spike in water pressure associated with the onset of transient moulin meltwater input up to and beyond 100% of overburden (Figure 3D–E) that is not evident further upglacier (e.g., Figure 3A). However, within 40–70 km from the ice margin and at the limit of channelisation, water pressure is consistently at or near overburden resulting in a band of high water pressure when plotted as a summer average (Figure 2A). Elsewhere water pressure remains lower in both winter and summer, reflecting i) the presence of channelised drainage efficiently evacuating water close to the ice margin (<40 km) during summer and the limited meltwater supply across the domain during winter. Further than 70 km from the ice margin, water pressure remains high throughout the year, rarely dropping below 75% (Figure 3C–E). We note that in the uncoupled configuration used here, GlaDS does not account for uplift of the overlying ice where water pressure exceeds 100% of overburden or the increase in cavity closure rates that would accompany the increase in basal velocity associated with such an uplift. In reality, sustained summer water pressure above and beyond overburden would result in the decoupling of the ice from the underlying bed necessary to explain the limited deformational structures within murtoo sediment exposures (e.g., Becher and Johnson, 2021; Mäkinen et al., 2023; Hovikoski et al., 2023).

The pattern of both channel discharge and sheet discharge within 40–60 km of the ice margin is also consistent with the development of the semi-efficient drainage system within which murtoos are hypothesised to form. Here, within meltwater routes (those both with and without murtoo fields), the median channel discharge approaches $\sim 10^0\ \mathrm{m^3\,s^{-1}}$ (e.g., Figure 4D), close to but never exceeding the critical discharge of channelisation as defined here ($Q_c = 1\ \mathrm{m^3\,s^{-1}}$). Channel discharge in these meltwater routes peaks months after the highest water pressure at the onset of the melt season, as cavity expansion promotes lower pressure and more efficient discharge that, in turn, is able to redirect more water from the sheet elements along pressure gradients. Channel discharge remains relatively high throughout the meltwater season, dropping only as meltwater supply diminishes through the following winter.

At several locations within the 40–60 km area of hypothesised murtoo formation, some element edges do pass the threshold discharge for channelisation throughout the melt season. Although GlaDS does not include a representation of broad and low canals (as described by Walder and Fowler, 1994) many of these low-discharge R-channels do align well with murtoo fields in the southwest and northeast portions of the FLDIL (e.g., Figure 3C). The median cross-sectional area of channels 40–60 km from the margin is 2.8 $\mathrm{m^2}$ (equivalent to a semi-circle with radius of 1.3 m), which suggest the limited cavity expansion within which murtoo sediments can accumulate is captured within our model, even if the radial geometry differs. Modelled channels do not always coincide with murtoo fields, particularly within the centre of our domain, 40–60 km from the ice margin. Here, our baseline scenario also reproduces apparent conditions for murtoo formation, including the termination of low-discharge channels and water pressures ≈100% over a broad area during summer (e.g., Figure 4E). Despite this, no murtoo fields have been mapped in this area (Ahokangas et al., 2021). The reason that murtoos are not present in an area of the FLDIL where our modelling suggests they should form may be due to limited sediment supply in and upglacier of this murtoo-free region. Sediment cover in this area is very thin, and the large areas of exposed bedrock likely limited the supply of sediment from which murtoos could form (Figure A1B), an interaction not yet accounted for in our modelling.

More broadly, modelled channels also compare well to geomorphological evidence of channelised drainage pathways beneath the FLIDL. Northern hemisphere glaciated Pleistocene terrains preserve an extensive record of subglacial landforms, and

https://doi.org/10.5194/egusphere-2023-2141
Preprint. Discussion started: 16 October 2023

in terrain formerly occupied by the Fennoscandian Ice Sheet (FIS) these landforms have been mapped and classified in detail (e.g., Ahokangas et al., 2021; Palmu et al., 2021; Dewald et al., 2021). In the FLDIL, besides numerous murtoo fields, large esker deposits also provide a useful means of evaluating model outputs (Figure 6). Although their exact mode of origin remains contentious (see Section 1), they are considered to largely represent deposition of sediment within subglacial channels beneath former ice sheets (Cofaigh, 1996; Greenwood et al., 2016). The location and characteristics of these landforms offer a useful means of evaluating model outputs from sensitivity tests. In several locations, modelled channel outputs in the baseline scenario closely track particularly large esker deposits mapped by Palmu et al. (2021) (Figure 6). Further, the $\sim$30 km horizontal spacing of larger eskers agrees well with modelled channel placement, and the observation that smaller eskers are interspersed amongst longer more continuous features (variable preservation notwithstanding) is similarly reproduced. Operating on an unstructured mesh, GlaDS is not subject to the same directional bias as grid-based models. Nonetheless, the exact location of channels is sensitive to mesh geometry. Altering the mesh does alter the exact placement of channels, however, the spacing of channels remains robust against the specifics of the various mesh geometries tested here (Figures A19, A20, A18). We also note that GlaDS successfully reproduces the distinction between meltwater routes (both with and without murtoos) and areas of the bed without any mapped meltwater routes (Figure 4). This, together with the similarity between mapped and modelled patterns of channelised drainage, suggest that GlaDS is faithfully capturing the broad patterns of drainage beneath the FLIDL.

Considered across the model domain, our results closely match the apparent spatiotemporal expression of channelisation in land-terminating sectors of the GrIS. In the base run Section 4.1, small channels ($1 \leq Q_c < 5\,\mathrm{m^3\,s^{-1}}$) extend up to a maximum of 60 km from the ice margin, where ice is between 1000–1100 m thick, and larger channels reach a maximum of 40 km inland ($\sim$850 m thick). Beneath the GrIS, tracer transit times indicate efficient channelisation reaches at least 41 km from the ice margin (Chandler et al., 2013). However, beyond this, thicker ice, which enhances creep closure, and shallower surface gradients which limit hydropotential gradients, likely inhibit channel growth (Röthlisberger, 1972; Davison et al., 2019). Previous modelling of the GrIS indicates the transition between channelised and distributed drainage occurs between ice 900–1200 m thick (Davison et al., 2019) with channelisation identified up to a maximum of 50 km from the ice margin, where ice is $\sim$900 m thick (De Fleurian et al., 2016) but absent 70 km from the ice margin beneath ice 1200 m thick (e.g., Dow et al., 2015).

On the GrIS, the upglacier propogation of rapid subglacial water velocities throughout the melt season (Chandler et al., 2013) and close correlation of proglacial discharge (Bartholomew et al., 2011) is linked to the development of channelised drainage (Davison et al., 2019). This process is considered analogous to that which occurs on Alpine glaciers (see Nienow et al., 1998) with meltwater delivered to the bed at high elevations initially encountering a distributed drainage system that becomes increasingly channelised with sustained meltwater delivery to the bed (Bartholomew et al., 2011). Similarly, the growth and decay of modelled channels here largely matches the seasonal evolution of those modelled and observed beneath the GrIS. Channels propagate up-glacier throughout the melt season and coalesce into fewer, larger, channels as the melt season progresses (Movie A1).

A notable difference between our model results and those beneath contemporary Greenland is the pressure conditions within large channels close to the margin. Beneath Greenland, channels form seasonally in response to meltwater discharge and exist at lower pressures than the surrounding distributed system (Davison et al., 2019). Such a hydraulic potential gradient forces large

https://doi.org/10.5194/egusphere-2023-2141
Preprint. Discussion started: 16 October 2023

volumes of water from the surrounding distributed system towards channels, in turn lowering water pressure in these systems and increasing basal traction (Schoof, 2010). As a result, despite increased meltwater delivery to the bed, these channels can act to reduce summer velocity (Nienow et al., 2017). In contrast, the channels modelled here remain at relatively high pressures throughout the year ($> 60\%$), with a lower hydraulic potential gradient between channelised and distributed systems. Although we run GlaDS here without any coupling to ice dynamics, it is likely that the influence of higher pressure channels on velocity would be more limited in such a system, with lower rates of exchange between distributed and channelised drainage permitting more of the bed to remain closer to overburden and sustaining higher velocities as a result (Dow et al., 2022).

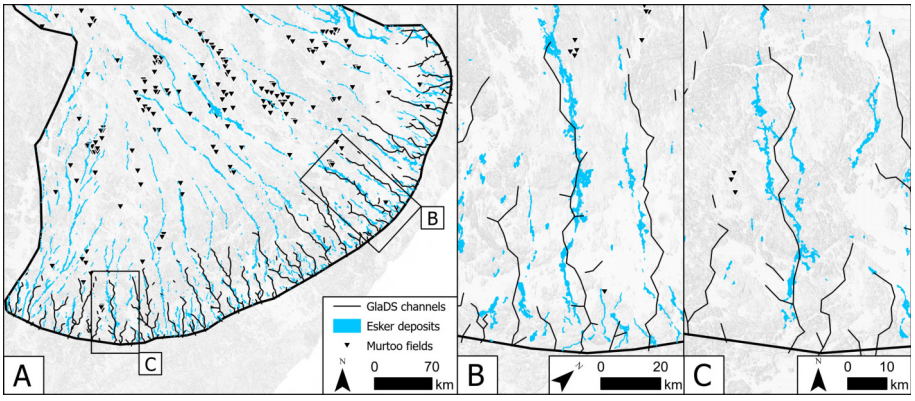

Figure 6. Modelled channel location compared to esker deposits mapped by Palmu et al. (2021) at the ice margin of the FLDIL. **A)** Modelled channels in the baseline run (black lines) across the full width of the domain against compared to esker deposits (blue polygons). **B & C)** Detailed comparison of two large esker systems against model channels.

Finally, we observe a biannual signal in our results, manifesting as both channel persistence through winter, as well as a statistically significant difference in the modelled characteristics of murtoo routes and meltwater routes without murtoos. In Greenland, winter slowdowns following high-melt summers have been linked to the sustained persistence of larger and more extensive channels into winter months (Sole et al., 2013). In our model, a biannual signal is evident in both channel persistence (e.g., Figures 3 & 2) and overburden within murtoo hosting meltwater routes (Figure 4). A number of channels persist through winter months, broadly following a pattern in which channels in the central third of the lobe will persist through alternating winters compared to those in the adjacent thirds (Movie A1). However, as described in Section 3.1 and following Werder et al. (2013), a minimum threshold $Q \geq 1\,\mathrm{m^3\,s^{-1}}$ was defined, above which an element edge was classified as a channel. Channels persisting through winter months tend to operate at very low discharges approaching $1\times10^{-6}\,\mathrm{m^3\,s^{-1}}$. Additionally our model forcing is cyclical but fixed year on year, and so this biannual pattern may arise due to internal model dynamics. A similarly repetitive biannual signal is considered unlikely in a system subject to more variable meltwater forcing. The observations that murtoo routes are generally absent from the centre of the FLDIL lobe and the alternating pattern of winter channel persistence between the central third and adjacent thirds of the lobe likely explains the significant difference in water pressure, discharge,

https://doi.org/10.5194/egusphere-2023-2141
Preprint. Discussion started: 16 October 2023

and velocity between murtoo routes (confined to the outer margins of the ice lobe) and meltwater routes without murtoos (distributed more evenly across the FLDIL, Figure A1A).

Although the biannual pattern of channel growth is likely driven by internal model dynamics and our fixed annual forcing, murtoos are observed to occur in discrete clusters along otherwise continuous meltwater routes (Ahokangas et al., 2021). Differential rates of feature preservation notwithstanding, such a discrete spatial expression may suggest the conditions necessary for murtoo formation were not met continuously throughout the retreat of the Fennoscandian Ice Sheet, rather they may occur periodically during or following extreme melt years. With a consistent rate of meltwater delivery between each model year, our modelling suggests that periodically elevated pressures can arise as a result of internal model dynamics alone, without any temporally variable forcing. Such internal model dynamics may include localised divergences in ice flow in our model. In the FLDIL, flow parallel lineations indicate a largely uniform flow direction within the primary trunk (e.g., Figure 1D) that diverges radially within the lobe. As a result, the FLDIL is divided into three sub-lobes, with the boundary between each demarcated by particularly large esker deposits (Palmu et al., 2021). These eskers and the sub-lobes they bound align approximately with the distinct alternating pattern of over-winter channel persistence, with channels persisting in years following the over winter persistence of central channels. Local deviation in ice flow direction may act as an initial perturbation which results in an initially enhanced meltwater delivery in the outer sub-lobes. We hypothesise that this locally enhanced discharge encourages the growth of channels large enough to resist the subsequent viscous creep closure in the following winter. In the following summer, more discharge is concentrated in these overwinter channels and water is more efficiently evacuated. Peak discharge is therefore met earlier in the season and these channels are subsequently exposed to longer periods in which creep closure exceeds channel growth. Simultaneously, because no channels persisted overwinter in the centre of the lobe, peak discharge is later in this region which results in late season discharge routed to the central channels and their persistence as these channels grow large enough to resist viscous creep closure overwinter. This initial perturbation and formation of overwinter channels creates an interannual cycle feedback that persists despite temporally fixed input. In our current model setup, without ice dynamics coupled to basal hydrology and with an annually fixed meltwater input, we cannot fully test this hypothesis further though it would be an interesting avenue for future study.

5.2 Limitations and future work

We make a number of simplifying assumptions to ensure models could run to completion within 1–2 days while remaining numerically stable across the range of parameters tested for model sensitivity. These include smoothing of the bed topography below the maximum resolution available, and using a relatively large mesh. However, sensitivity testing indicates our conclusions are largely insensitive to topography, including its absence, and that the ice surface gradient instead imposes the dominant control on basal hydrology. Similarly, changing the mesh resolution also appears to have limited impact on our conclusions. We did not account for changes in elevation due to glacial isostatic adjustment (GIA) since 12 $\mathrm{cal.\,ka}$. Accounting for an anticipated uplift and tilting in this area of $\sim$100 m (Ojala et al., 2013; Rosentau et al., 2021) is likely to increase the volume of melt delivered to the bed by elevating the mean annual air temperature by $\sim$0.75°C near to the ice margin, which will result in higher discharge channels that persist further upglacier. However, we do not anticipate this will significantly alter our conclusions.

https://doi.org/10.5194/egusphere-2023-2141
Preprint. Discussion started: 16 October 2023

Additional uncertainty arises from our estimated (and constant) meltwater and basal melt inputs, fixed basal velocity, fixed conductivity parameters (in both space and time), lack of ice deformation in response to negative effective pressures, assumed water turbulence, lack of water flux input from abutting ice, and randomly seeded moulin inputs. Future work will seek to address some of these limitations by including, for example, coupled ice dynamics which are allowed to vary in response to effective pressure (e.g., as in Ehrenfeucht et al., 2023). Initial sensitivity testing of velocity forced to change seasonally does indicate that changes in velocity throughout the year is important for repressurising the system each winter to more closely match borehole records (e.g., Doyle et al., 2018, 2022). Considering each of these limitations our results therefore describe the seasonal evolution of channelised and distributed drainage system beneath a necessarily idealised representation of our study site in the FLDIL. However, we emphasise that our results suggest that the approach of examining palaeo basal topography alongside subglacial hydrology model outputs holds promise for mutually beneficial analyses of palaeo and contemporary ice sheets to assess the controls of hydrology on ice dynamics and subglacial landform evolution.

6 Conclusions

We successfully reproduce the macro conditions associated with murtoo formation by applying GlaDS, a dynamic model of basal hydrology, to the palaeo Finnish Lake District Ice Lobe (FLDIL) forced by a positive degree day model. Our model was parameterised using high-resolution digital elevation models, modified to approximate the terrain during the Younger Dryas $\sim$12 cal. ka, together with a model representation of ice surface elevation for the same time period. By sensitivity testing a range of parameters difficult to measure, including conductivity and moulin density, we demonstrate that murtoo genesis is consistent with their formation 40–60 km from the ice margin at the onset of channelisation, where water pressure is consistently at or near overburden pressure during summer. Our modelling reproduces the concentration of meltwater into discrete channels, matching the approximate spacing and characteristics of geomorphology such as eskers. The spatial distribution of murtoos, which are present in discontinuous fields within otherwise continuous meltwater routes, may arise following consecutive years of elevated meltwater volumes. Although our system is necessarily an idealised representation of the study site, not including adjacent and abutting ice lobes, an upstream catchment area, or a coupled representation of ice dynamics and basal hydrology, this work nonetheless demonstrates the potential for basal hydrology modelling in the palaeo setting, where model outputs can be directly compared to geomorphology.

Code and data availability. All geophysical data used to parameterise the modelling (e.g., Quaternary sediment thickness, geothermal heat flux, lake bathymetry) is available from Finnish Geological Survey's 'Hakku' service (https://hakku.gtk.fi/?locale=en, last accessed on 06-09-2023). The Copernicus DEM used as basal elevation is available from: https://spacedata.copernicus.eu/collections/copernicus-digital-elevation-model (last accessed on 06-09-2023). For our modelling we used the Ice-sheet and Sea-level System Model (Larour et al., 2012) `revision 27448` available from: https://issm.jpl.nasa.gov/ (last accessed on 06-09-2023). Murtoo field locations from Ahokangas et al. (2021), glacial landforms shapefile data from Palmu et al. (2021), model results, and example input scripts used to produce and plot those results are available at the repository linked to this manuscript (https://doi.org/10.5281/zenodo.8344208, Hepburn et al., 2023)

https://doi.org/10.5194/egusphere-2023-2141
Preprint. Discussion started: 16 October 2023

Video supplement. Movie A1 is available at the online repository linked to this article (https://doi.org/10.5281/zenodo.8344208, Hepburn et al., 2023).

Author contributions. A.O, J.M, and C.F.D conceived the study, A.J.H designed and carried out the study and wrote the manuscript, all authors commented on the writing and helped with the analysis and interpretation.

Competing interests. The authors declare that no competing interests are present

Acknowledgements. This work forms part of the RewarD project (MUST consortium, University of Turku), funded by the Academy of Finland (grant numbers 322243/J.M and 322252/A.O). A.J.H is funded by the European Space Agency Internal Fellowship program, C.F.D is funded by the Canada Research Chair program (950-231237). All simulations were run on the Digital Research Alliance of Canada compute cluster, and we thank the European Union and the Finnish Geological Survey for enabling access to the data used to parameterise our model. We thank M.Werder for making the GlaDS model available, and we also thank M. Morlighem, J. Quinn, and J. Cuzzone for their help with ISSM.

https://doi.org/10.5194/egusphere-2023-2141
Preprint. Discussion started: 16 October 2023

References

Abatzoglou, J. T., Dobrowski, S. Z., Parks, S. A., and Hegewisch, K. C.: TerraClimate, a high-resolution global dataset of monthly climate and climatic water balance from 1958–2015, Scientific data, 5, 1–12, 2018.

Ahokangas, E., Ojala, A. E., Tuunainen, A., Valkama, M., Palmu, J.-P., Kajuutti, K., and Mäkinen, J.: The distribution of glacial meltwater routes and associated murtoo fields in Finland, Geomorphology, 389, 107 854, 2021.

Åkesson, H., Morlighem, M., Nisancioglu, K. H., Svendsen, J. I., and Mangerud, J.: Atmosphere-driven ice sheet mass loss paced by topography: Insights from modelling the south-western Scandinavian Ice Sheet, Quaternary Science Reviews, 195, 32–47, 2018.

Arnold, N.: A new approach for dealing with depressions in digital elevation models when calculating flow accumulation values, Progress in Physical Geography, 34, 781–809, 2010.

Banwell, A. F., Willis, I. C., and Arnold, N. S.: Modeling subglacial water routing at Paakitsoq, W Greenland, Journal of Geophysical Research: Earth Surface, 118, 1282–1295, 2013.

Bartholomew, I., Nienow, P., Sole, A., Mair, D., Cowton, T., Palmer, S., and Wadham, J.: Supraglacial forcing of subglacial drainage in the ablation zone of the Greenland ice sheet, Geophysical Research Letters, 38, 2011.

Bartholomew, I., Nienow, P., Sole, A., Mair, D., Cowton, T., and King, M. A.: Short-term variability in Greenland Ice Sheet motion forced by time-varying meltwater drainage: Implications for the relationship between subglacial drainage system behavior and ice velocity, Journal of Geophysical Research: Earth Surface, 117, 2012.

Becher, G. P. and Johnson, M. D.: Sedimentology and internal structure of murtoos-V-shaped landforms indicative of a dynamic subglacial hydrological system, Geomorphology, 380, 107 644, 2021.

Boswell, S. M., Toucanne, S., Pitel-Roudaut, M., Creyts, T. T., Eynaud, F., and Bayon, G.: Enhanced surface melting of the Fennoscandian Ice Sheet during periods of North Atlantic cooling, Geology, 47, 664–668, 2019.

Boulton, G. and Jones, A.: Stability of temperate ice caps and ice sheets resting on beds of deformable sediment, Journal of Glaciology, 24, 29–43, 1979.

Boulton, G. S., Dongelmans, P., Punkari, M., and Broadgate, M.: Palaeoglaciology of an ice sheet through a glacial cycle:: the European ice sheet through the Weichselian, Quaternary Science Reviews, 20, 591–625, 2001.

Braithwaite, R. J. and Olesen, O. B.: Calculation of glacier ablation from air temperature, West Greenland, in: Glacier Fluctuations and Climatic Change: Proceedings of the Symposium on Glacier Fluctuations and Climatic Change, held in Amsterdam, 1–5 June 1987, pp. 219–233, Springer, 1989.

Brennand, T. A.: Deglacial meltwater drainage and glaciodynamics: inferences from Laurentide eskers, Canada, Geomorphology, 32, 263–293, 2000.

Budd, W., Keage, P., and Blundy, N.: Empirical studies of ice sliding, Journal of glaciology, 23, 157–170, 1979.

Carter, S. P., Fricker, H. A., and Siegfried, M. R.: Antarctic subglacial lakes drain through sediment-floored canals: theory and model testing on real and idealized domains, The Cryosphere, 11, 381–405, 2017.

Chandler, D., Wadham, J., Lis, G., Cowton, T., Sole, A., Bartholomew, I., Telling, J., Nienow, P., Bagshaw, E., Mair, D., et al.: Evolution of the subglacial drainage system beneath the Greenland Ice Sheet revealed by tracers, Nature Geoscience, 6, 195–198, 2013.

Chandler, D. M., Wadham, J. L., Nienow, P. W., Doyle, S. H., Tedstone, A. J., Telling, J., Hawkings, J., Alcock, J. D., Linhoff, B., and Hubbard, A.: Rapid development and persistence of efficient subglacial drainage under 900 m-thick ice in Greenland, Earth and Planetary Science Letters, 566, 116 982, 2021.

https://doi.org/10.5194/egusphere-2023-2141
Preprint. Discussion started: 16 October 2023

Chapwanya, M., Clark, C. D., and Fowler, A. C.: Numerical computations of a theoretical model of ribbed moraine formation, Earth Surface Processes and Landforms, 36, 1105–1112, 2011.

Chu, W., Creyts, T. T., and Bell, R. E.: Rerouting of subglacial water flow between neighboring glaciers in West Greenland, Journal of Geophysical Research: Earth Surface, 121, 925–938, 2016.

Clark, C. D., Chiverrell, R. C., Fabel, D., Hindmarsh, R. C., Ó Cofaigh, C., and Scourse, J. D.: Timing, pace and controls on ice sheet retreat: an introduction to the BRITICE-CHRONO transect reconstructions of the British–Irish Ice Sheet, Journal of Quaternary Science, 36, 673–680, 2021.

Clark, P. U. and Walder, J. S.: Subglacial drainage, eskers, and deforming beds beneath the Laurentide and Eurasian ice sheets, Geological Society of America Bulletin, 106, 304–314, 1994.

Cofaigh, C. Ó.: Tunnel valley genesis, Progress in physical geography, 20, 1–19, 1996.

Cook, S., Christoffersen, P., Todd, J., Slater, D., and Chauché, N.: Integrated investigation of subglacial hydrology and convective plume melting using a 3D full-Stokes model of Store Glacier, West Greenland., in: Geophysical Research Abstracts, vol. 21, 2019.

Cook, S. J., Christoffersen, P., Todd, J., Slater, D., and Chauché, N.: Coupled modelling of subglacial hydrology and calving-front melting at Store Glacier, West Greenland, The Cryosphere, 14, 905–924, 2020.

Cook, S. J., Christoffersen, P., and Todd, J.: A fully-coupled 3D model of a large Greenlandic outlet glacier with evolving subglacial hydrology, frontal plume melting and calving, Journal of Glaciology, 68, 486–502, 2022.

Coughlan, M., Tóth, Z., Van Landeghem, K. J., Mccarron, S., and Wheeler, A. J.: Formational history of the Wicklow Trough: a marine-transgressed tunnel valley revealing ice flow velocity and retreat rates for the largest ice stream draining the late-Devensian British–Irish Ice Sheet, Journal of Quaternary Science, 35, 907–919, 2020.

Cowton, T., Nienow, P., Sole, A., Wadham, J., Lis, G., Bartholomew, I., Mair, D., and Chandler, D.: Evolution of drainage system morphology at a land-terminating Greenlandic outlet glacier, Journal of Geophysical Research: Earth Surface, 118, 29–41, 2013.

Cuffey, K. M. and Paterson, W. S. B.: The physics of glaciers, Academic Press, 2010.

Cuzzone, J. K., Schlegel, N.-J., Morlighem, M., Larour, E., Briner, J. P., Seroussi, H., and Caron, L.: The impact of model resolution on the simulated Holocene retreat of the southwestern Greenland ice sheet using the Ice Sheet System Model (ISSM), The Cryosphere, 13, 879–893, 2019.

Davison, B. J., Sole, A. J., Livingstone, S. J., Cowton, T. R., and Nienow, P. W.: The influence of hydrology on the dynamics of land-terminating sectors of the Greenland ice sheet, Frontiers in Earth Science, 7, 10, 2019.

De Fleurian, B., Morlighem, M., Seroussi, H., Rignot, E., van den Broeke, M. R., Kuipers Munneke, P., Mouginot, J., Smeets, P. C., and Tedstone, A. J.: A modeling study of the effect of runoff variability on the effective pressure beneath Russell Glacier, West Greenland, Journal of Geophysical Research: Earth Surface, 121, 1834–1848, 2016.

Dewald, N., Lewington, E. L., Livingstone, S. J., Clark, C. D., and Storrar, R. D.: Distribution, characteristics and formation of esker enlargements, Geomorphology, 392, 107 919, 2021.

Dewald, N., Livingstone, S. J., and Clark, C. D.: Subglacial meltwater routes of the Fennoscandian Ice Sheet, Journal of Maps, 18, 382–396, 2022.

Donner, J.: The Younger Dryas age of the Salpausselkä moraines in Finland, Bulletin of the Geological Society of Finland, 82, 69–80, 2010.

Dow, C., Werder, M., Nowicki, S., and Walker, R.: Modeling Antarctic subglacial lake filling and drainage cycles., Cryosphere Discussions, 9, 2015.

https://doi.org/10.5194/egusphere-2023-2141
Preprint. Discussion started: 16 October 2023

Dow, C., McCormack, F., Young, D., Greenbaum, J., Roberts, J., and Blankenship, D.: Totten Glacier subglacial hydrology determined from geophysics and modeling, Earth and Planetary Science Letters, 531, 115 961, 2020.

Dow, C., Ross, N., Jeofry, H., Siu, K., and Siegert, M.: Antarctic basal environment shaped by high-pressure flow through a subglacial river system, Nature Geoscience, 15, 892–898, 2022.

Dow, C. F.: The role of subglacial hydrology in Antarctic ice sheet dynamics and stability: a modelling perspective, Annals of Glaciology, pp. 1–6, 2023.

Dow, C. F., Karlsson, N. B., and Werder, M. A.: Limited impact of subglacial supercooling freeze-on for Greenland ice sheet stratigraphy, Geophysical Research Letters, 45, 1481–1489, 2018a.

Dow, C. F., Lee, W. S., Greenbaum, J. S., Greene, C. A., Blankenship, D. D., Poinar, K., Forrest, A. L., Young, D. A., and Zappa, C. J.: Basal channels drive active surface hydrology and transverse ice shelf fracture, Science Advances, 4, eaao7212, 2018b.

Dow, C. F., Werder, M., Babonis, G., Nowicki, S., Walker, R. T., Csathó, B., and Morlighem, M.: Dynamics of active subglacial lakes in Recovery Ice Stream, Journal of Geophysical Research: Earth Surface, 123, 837–850, 2018c.

Doyle, S. H., Hubbard, B., Christoffersen, P., Young, T. J., Hofstede, C., Bougamont, M., Box, J., and Hubbard, A.: Physical conditions of fast glacier flow: 1. Measurements from boreholes drilled to the bed of Store Glacier, West Greenland, Journal of Geophysical Research: Earth Surface, 123, 324–348, 2018.

Doyle, S. H., Hubbard, B., Christoffersen, P., Law, R., Hewitt, D. R., Neufeld, J. A., Schoonman, C. M., Chudley, T. R., and Bougamont, M.: Water flow through sediments and at the ice-sediment interface beneath Sermeq Kujalleq (Store Glacier), Greenland, Journal of Glaciology, 68, 665–684, 2022.

Ehrenfeucht, S., Morlighem, M., Rignot, E., Dow, C. F., and Mouginot, J.: Seasonal acceleration of Petermann Glacier, Greenland, from changes in subglacial hydrology, Geophysical Research Letters, 50, e2022GL098 009, 2023.

Fausto, R. S., Ahlstrøm, A. P., Van As, D., and Steffen, K.: Present-day temperature standard deviation parameterization for Greenland, Journal of Glaciology, 57, 1181–1183, 2011.

Flowers, G. E.: Hydrology and the future of the Greenland Ice Sheet, Nature communications, 9, 2729, 2018.

Fowler, A.: The formation of subglacial streams and mega-scale glacial lineations, Proceedings of the Royal Society A: Mathematical, Physical and Engineering Sciences, 466, 3181–3201, 2010.

Fowler, A. C. and Chapwanya, M.: An instability theory for the formation of ribbed moraine, drumlins and mega-scale glacial lineations, Proceedings of the Royal Society A: Mathematical, Physical and Engineering Sciences, 470, 20140 185, 2014.

Gardner, A. S., Sharp, M. J., Koerner, R. M., Labine, C., Boon, S., Marshall, S. J., Burgess, D. O., and Lewis, D.: Near-surface temperature lapse rates over Arctic glaciers and their implications for temperature downscaling, Journal of Climate, 22, 4281–4298, 2009.

Greenwood, S. L., Clason, C. C., Helanow, C., and Margold, M.: Theoretical, contemporary observational and palaeo-perspectives on ice sheet hydrology: processes and products, Earth-Science Reviews, 155, 1–27, 2016.

Greenwood, S. L., Clason, C. C., Nyberg, J., Jakobsson, M., and Holmlund, P.: The Bothnian Sea ice stream: early Holocene retreat dynamics of the south-central Fennoscandian Ice Sheet, Boreas, 46, 346–362, 2017.

GTK, Finland: Superficial deposits of Finland 1:200 000 (sediment polygons), https://tupa.gtk.fi/paikkatieto/meta/maapera_200k.html#tunnistamistiedo, 2010.

Hager, A. O., Hoffman, M. J., Price, S. F., and Schroeder, D. M.: Persistent, extensive channelized drainage modeled beneath Thwaites Glacier, West Antarctica, The Cryosphere, 16, 3575–3599, 2022.

https://doi.org/10.5194/egusphere-2023-2141
Preprint. Discussion started: 16 October 2023

Harper, J., Meierbachtol, T., Humphrey, N., Saito, J., and Stansberry, A.: Generation and fate of basal meltwater during winter, western Greenland Ice Sheet, The Cryosphere, 15, 5409–5421, 2021.

Hepburn, A., Dow, C., Ojala, A., Mäkinen, J., Ahokangas, E., Hovikoski, J., Jukka-Pekka, P., and Kajuutti, K.: Supplementary material for 'Reorganisation of subglacial drainage processes during rapid melting of the Fennoscandian Ice Sheet, https://doi.org/10.5281/zenodo.8344208, 2023.

Hooke, R. L.: Englacial and subglacial hydrology: a qualitative review, Arctic and Alpine Research, 21, 221–233, 1989.

Hooke, R. L. and Fastook, J.: Thermal conditions at the bed of the Laurentide ice sheet in Maine during deglaciation: implications for esker formation, Journal of Glaciology, 53, 646–658, 2007.

Hooke, R. L. and Jennings, C. E.: On the formation of the tunnel valleys of the southern Laurentide ice sheet, Quaternary Science Reviews, 25, 1364–1372, 2006.

Hovikoski, J., Mäkinen, J., Winsemann, J., Soini, S., Kajuutti, K., Hepburn, A., and Ojala, A.: Upper-flow regime bedforms in a subglacial triangular-shaped landform (murtoo), late Pleistocene, SW Finland: Implications for flow dynamics and sediment transport in (semi-) distributed subglacial meltwater drainage systems, Sedimentary Geology, p. 106448, 2023.

Hubbard, B., Sharp, M., Willis, I., Nielsen, M., and Smart, C.: Borehole water-level variations and the structure of the subglacial hydrological system of Haut Glacier dArolla, Valais, Switzerland, Journal of Glaciology, 41, 572–583, 1995.

Hughes, A. L., Gyllencreutz, R., Lohne, Ø. S., Mangerud, J., and Svendsen, J. I.: The last Eurasian ice sheets–a chronological database and time-slice reconstruction, DATED-1, Boreas, 45, 1–45, 2016.

Iken, A. and Bindschadler, R. A.: Combined measurements of subglacial water pressure and surface velocity of Findelengletscher, Switzerland: conclusions about drainage system and sliding mechanism, Journal of Glaciology, 32, 101–119, 1986.

Indrigo, C., Dow, C. F., Greenbaum, J. S., and Morlighem, M.: Drygalski Ice Tongue stability influenced by rift formation and ice morphology, Journal of Glaciology, 67, 243–252, 2021.

Iverson, N. R., Baker, R. W., Hooke, R. L., Hanson, B., and Jansson, P.: Coupling between a glacier and a soft bed: I. A relation between effective pressure and local shear stress determined from till elasticity, Journal of Glaciology, 45, 31–40, 1999.

Johansson, P., Kujansuu, R., Eriksson, B., Grönlund, T., Johansson, P., Kejonen, A., Kujansuu, R., Maunu, M., Mäkinen, K., Saarnisto, M., et al.: Pohjois-Suomen maaperä: maaperäkarttojen 1: 400 000 selitys, Summary: Quaternary deposits of Northern Finland–Explanation to the maps of Quaternary deposits, 1, 000, 2005.

Johnsen, S. J., Clausen, H. B., Dansgaard, W., Gundestrup, N. S., Hammer, C. U., Andersen, U., Andersen, K. K., Hvidberg, C. S., Dahl-Jensen, D., Steffensen, J. P., et al.: The δ18O record along the Greenland Ice Core Project deep ice core and the problem of possible Eemian climatic instability, Journal of Geophysical Research: Oceans, 102, 26 397–26 410, 1997.

Joughin, I., Das, S. B., King, M. A., Smith, B. E., Howat, I. M., and Moon, T.: Seasonal speedup along the western flank of the Greenland Ice Sheet, Science, 320, 781–783, 2008.

Kamb, B.: Glacier surge mechanism based on linked cavity configuration of the basal water conduit system, Journal of Geophysical Research: Solid Earth, 92, 9083–9100, 1987.

Karlsson, N. B. and Dahl-Jensen, D.: Response of the large-scale subglacial drainage system of Northeast Greenland to surface elevation changes, The Cryosphere, 9, 1465–1479, 2015.

Karlsson, N. B., Solgaard, A. M., Mankoff, K. D., Gillet-Chaulet, F., MacGregor, J. A., Box, J. E., Citterio, M., Colgan, W. T., Larsen, S. H., Kjeldsen, K. K., et al.: A first constraint on basal melt-water production of the Greenland ice sheet, Nature Communications, 12, 3461, 2021.

https://doi.org/10.5194/egusphere-2023-2141
Preprint. Discussion started: 16 October 2023

Killingbeck, S. F., Booth, A. D., Livermore, P. W., Bates, C. R., and West, L. J.: Characterisation of subglacial water using a constrained transdimensional Bayesian transient electromagnetic inversion, Solid Earth, 11, 75–94, 2020.

Kirkham, J. D., Hogan, K. A., Larter, R. D., Arnold, N. S., Ely, J. C., Clark, C. D., Self, E., Games, K., Huuse, M., Stewart, M. A., et al.: Tunnel valley formation beneath deglaciating mid-latitude ice sheets: Observations and modelling, Quaternary Science Reviews, p. 107680, 2022.

Kleman, J., Hättestrand, C., Borgström, I., and Stroeven, A.: Fennoscandian palaeoglaciology reconstructed using a glacial geological inversion model, Journal of glaciology, 43, 283–299, 1997.

Larour, E., Seroussi, H., Morlighem, M., and Rignot, E.: Continental scale, high order, high spatial resolution, ice sheet modeling using the Ice Sheet System Model (ISSM), Journal of Geophysical Research: Earth Surface, 117, 2012.

Lehtinen, M., Nurmi, P. A., and Ramo, O.: Precambrian Geology of Finland, Elsevier, 2005.

Lewington, E. L., Livingstone, S. J., Sole, A. J., Clark, C. D., and Ng, F. S.: An automated method for mapping geomorphological expressions of former subglacial meltwater pathways (hummock corridors) from high resolution digital elevation data, Geomorphology, 339, 70–86, 2019.

Livingstone, S., Clark, C., Woodward, J., and Kingslake, J.: Potential subglacial lakes and meltwater drainage pathways beneath the Antarctic and Greenland ice sheets, The Cryosphere, 7, 1721–1740, 2013a.

Livingstone, S. J., Clark, C. D., and Tarasov, L.: Modelling North American palaeo-subglacial lakes and their meltwater drainage pathways, Earth and Planetary Science Letters, 375, 13–33, 2013b.

Livingstone, S. J., Storrar, R. D., Hillier, J. K., Stokes, C. R., Clark, C. D., and Tarasov, L.: An ice-sheet scale comparison of eskers with modelled subglacial drainage routes, Geomorphology, 246, 104–112, 2015.

Lunkka, J. P., Johansson, P., Saarnisto, M., and Sallasmaa, O.: Glaciation of Finland, in: Developments in Quaternary Sciences, vol. 2, pp. 93–100, Elsevier, 2004.

Lunkka, J. P., Palmu, J.-P., and Seppänen, A.: Deglaciation dynamics of the Scandinavian Ice Sheet in the Salpausselkä zone, southern Finland, Boreas, 50, 404–418, 2021.

MacAyeal, D. R.: Large-scale ice flow over a viscous basal sediment: Theory and application to ice stream B, Antarctica, Journal of Geophysical Research: Solid Earth, 94, 4071–4087, 1989.

Mair, D., Nienow, P., Sharp, M., Wohlleben, T., and Willis, I.: Influence of subglacial drainage system evolution on glacier surface motion: Haut Glacier d'Arolla, Switzerland, Journal of Geophysical Research: Solid Earth, 107, EPM–8, 2002.

Mair, D., Willis, I., Fischer, U. H., Hubbard, B., Nienow, P., and Hubbard, A.: Hydrological controls on patterns of surface, internal and basal motion during three spring events: Haut Glacier dArolla, Switzerland, Journal of Glaciology, 49, 555–567, 2003.

Mäkinen, J.: Time-transgressive deposits of repeated depositional sequences within interlobate glaciofluvial (esker) sediments in Köyliö, SW Finland, Sedimentology, 50, 327–360, 2003.

Mäkinen, J., Kajuutti, K., Palmu, J.-P., Ojala, A., and Ahokangas, E.: Triangular-shaped landforms reveal subglacial drainage routes in SW Finland, Quaternary Science Reviews, 164, 37–53, 2017.

Mäkinen, J., Kajuutti, K., Ojala, A. E., Ahokangas, E., Tuunainen, A., Valkama, M., and Palmu, J.-P.: Genesis of subglacial triangular-shaped landforms (murtoos) formed by the Fennoscandian Ice Sheet, Earth Surface Processes and Landforms, 2023.

Marshall, S. J. and Sharp, M. J.: Temperature and melt modeling on the Prince of Wales ice field, Canadian High Arctic, Journal of Climate, 22, 1454–1468, 2009.

https://doi.org/10.5194/egusphere-2023-2141
Preprint. Discussion started: 16 October 2023

McArthur, K., McCormack, F. S., and Dow, C. F.: Basal conditions of Denman Glacier from glacier hydrology and ice dynamics modeling, The Cryosphere Discussions, pp. 1–29, 2023.

Meierbachtol, T., Harper, J., and Humphrey, N.: Basal drainage system response to increasing surface melt on the Greenland ice sheet, Science, 341, 777–779, 2013.

Moon, T., Joughin, I., Smith, B., Van Den Broeke, M. R., Van De Berg, W. J., Noël, B., and Usher, M.: Distinct patterns of seasonal Greenland glacier velocity, Geophysical research letters, 41, 7209–7216, 2014.

Morlighem, M., Williams, C. N., Rignot, E., An, L., Arndt, J. E., Bamber, J. L., Catania, G., Chauché, N., Dowdeswell, J. A., Dorschel, B., et al.: BedMachine v3: Complete bed topography and ocean bathymetry mapping of Greenland from multibeam echo sounding combined with mass conservation, Geophysical research letters, 44, 11–051, 2017.

Morlighem, M., Rignot, E., Binder, T., Blankenship, D., Drews, R., Eagles, G., Eisen, O., Ferraccioli, F., Forsberg, R., Fretwell, P., et al.: Deep glacial troughs and stabilizing ridges unveiled beneath the margins of the Antarctic ice sheet, Nature Geoscience, 13, 132–137, 2020.

Nick, F. M., Vieli, A., Andersen, M. L., Joughin, I., Payne, A., Edwards, T. L., Pattyn, F., and van de Wal, R. S.: Future sea-level rise from Greenlands main outlet glaciers in a warming climate, Nature, 497, 235–238, 2013.

Nienow, P., Sharp, M., and Willis, I.: Seasonal changes in the morphology of the subglacial drainage system, Haut Glacier d'Arolla, Switzerland, Earth Surface Processes and Landforms: The Journal of the British Geomorphological Group, 23, 825–843, 1998.

Nienow, P., Sole, A., Slater, D. A., and Cowton, T.: Recent advances in our understanding of the role of meltwater in the Greenland Ice Sheet system, Current Climate Change Reports, 3, 330–344, 2017.

Nye, J.: Water at the bed of a glacier, in: International Glaciological Society, pp. 189–194, 1972.

Ojala, A. E., Palmu, J.-P., Åberg, A., Åberg, S., and Virkki, H.: Development of an ancient shoreline database to reconstruct the Litorina Sea maximum extension and the highest shoreline of the Baltic Sea basin in Finland, Bulletin of the Geological Society of Finland, 2013.

Ojala, A. E., Peterson, G., Mäkinen, J., Johnson, M. D., Kajuutti, K., Palmu, J.-P., Ahokangas, E., and Öhrling, C.: Ice-sheet scale distribution and morphometry of triangular-shaped hummocks (murtoos): a subglacial landform produced during rapid retreat of the Scandinavian Ice Sheet, Annals of Glaciology, 60, 115–126, 2019.

Ojala, A. E., Mäkinen, J., Ahokangas, E., Kajuutti, K., Valkama, M., Tuunainen, A., and Palmu, J.-P.: Diversity of murtoos and murtoo-related subglacial landforms in the Finnish area of the Fennoscandian Ice Sheet, Boreas, 50, 1095–1115, 2021.

Ojala, A. E., Mäkinen, J., Kajuutti, K., Ahokangas, E., and Palmu, J.-P.: Subglacial evolution from distributed to channelized drainage: evidence from the Lake Murtoo area in SW Finland, Earth Surface Processes and Landforms, 47, 2877–2896, 2022.

Palmu, J.-P., Ojala, A. E., Virtasalo, J., Putkinen, N., Kohonen, J., and Sarala, P.: Classification system of superficial (quaternary) geological units in Finland, Developments in Map Data Management and Geological Unit Nomenclature in Finland, 412, 115–169, 2021.

Patton, H., Hubbard, A., Andreassen, K., Auriac, A., Whitehouse, P. L., Stroeven, A. P., Shackleton, C., Winsborrow, M., Heyman, J., and Hall, A. M.: Deglaciation of the Eurasian ice sheet complex, Quaternary Science Reviews, 169, 148–172, 2017.

Peterson, G., Johnson, M. D., and Smith, C. A.: Glacial geomorphology of the south Swedish uplands–focus on the spatial distribution of hummock tracts, Journal of Maps, 13, 534–544, 2017.

Poinar, K., Dow, C. F., and Andrews, L. C.: Long-term support of an active subglacial hydrologic system in Southeast Greenland by firn aquifers, Geophysical Research Letters, 46, 4772–4781, 2019.

Punkari, M.: The ice lobes of the Scandinavian ice sheet during the deglaciation in Finland., Boreas, 9, 307–310, 1980.

Punkari, M.: Subglacial processes of the Scandinavian Ice Sheet in Fennoscandia inferred from flow-parallel features and lithostratigraphy, Sedimentary Geology, 111, 263–283, 1997.

https://doi.org/10.5194/egusphere-2023-2141
Preprint. Discussion started: 16 October 2023

Putkinen, N., Eyles, N., Putkinen, S., Ojala, A. E., Palmu, J.-P., Sarala, P., Väänänen, T., Räisänen, J., Saarelainen, J., Ahtonen, N., et al.: High-resolution LiDAR mapping of glacial landforms and ice stream lobes in Finland., Bulletin of the Geological Society of Finland, 89, 2017.

Rampton, V.: Large-scale effects of subglacial meltwater flow in the southern Slave Province, Northwest Territories, Canada, Canadian Journal of Earth Sciences, 37, 81–93, 2000.

Regnéll, C., Mangerud, J., and Svendsen, J. I.: Tracing the last remnants of the Scandinavian Ice Sheet: Ice-dammed lakes and a catastrophic outburst flood in northern Sweden, Quaternary Science Reviews, 221, 105 862, 2019.

Rosentau, A., Klemann, V., Bennike, O., Steffen, H., Wehr, J., Latinović, M., Bagge, M., Ojala, A., Berglund, M., Becher, G. P., et al.: A Holocene relative sea-level database for the Baltic Sea, Quaternary Science Reviews, 266, 107 071, 2021.

Röthlisberger, H.: Water pressure in intra-and subglacial channels, Journal of Glaciology, 11, 177–203, 1972.

Salonen, V.-P.: Glacial transport distance distributions of surface boulders in Finland, Bulletin-Geological survey of Finland, 1986.

Scholzen, C., Schuler, T. V., and Gilbert, A.: Sensitivity of subglacial drainage to water supply distribution at the Kongsfjord basin, Svalbard, The Cryosphere, 15, 2719–2738, 2021.

Schoof, C.: The effect of cavitation on glacier sliding, Proceedings of the Royal Society A: Mathematical, Physical and Engineering Sciences, 461, 609–627, 2005.

Schoof, C.: Ice-sheet acceleration driven by melt supply variability, Nature, 468, 803–806, 2010.

Shackleton, C., Patton, H., Hubbard, A., Winsborrow, M., Kingslake, J., Esteves, M., Andreassen, K., and Greenwood, S. L.: Subglacial water storage and drainage beneath the Fennoscandian and Barents Sea ice sheets, Quaternary Science Reviews, 201, 13–28, 2018.

Sole, A., Nienow, P., Bartholomew, I., Mair, D., Cowton, T., Tedstone, A., and King, M. A.: Winter motion mediates dynamic response of the Greenland Ice Sheet to warmer summers, Geophysical Research Letters, 40, 3940–3944, 2013.

Sole, A. J., Mair, D. W. F., Nienow, P. W., Bartholomew, I., King, M., Burke, M. J., and Joughin, I.: Seasonal speedup of a Greenland marine-terminating outlet glacier forced by surface melt–induced changes in subglacial hydrology, Journal of Geophysical Research: Earth Surface, 116, 2011.

Stokes, C. R., Fowler, A. C., Clark, C. D., Hindmarsh, R. C., and Spagnolo, M.: The instability theory of drumlin formation and its explanation of their varied composition and internal structure, Quaternary Science Reviews, 62, 77–96, 2013.

Storrar, R. D. and Livingstone, S. J.: Glacial geomorphology of the northern Kivalliq region, Nunavut, Canada, with an emphasis on meltwater drainage systems, Journal of Maps, 13, 153–164, 2017.

Storrar, R. D., Stokes, C. R., and Evans, D. J.: Increased channelization of subglacial drainage during deglaciation of the Laurentide Ice Sheet, Geology, 42, 239–242, 2014.

Stroeven, A. P., Hättestrand, C., Kleman, J., Heyman, J., Fabel, D., Fredin, O., Goodfellow, B. W., Harbor, J. M., Jansen, J. D., Olsen, L., et al.: Deglaciation of fennoscandia, Quaternary Science Reviews, 147, 91–121, 2016.

Tuckett, P. A., Ely, J. C., Sole, A. J., Livingstone, S. J., Davison, B. J., Melchior van Wessem, J., and Howard, J.: Rapid accelerations of Antarctic Peninsula outlet glaciers driven by surface melt, Nature Communications, 10, 4311, 2019.

Utting, D. J., Ward, B. C., and Little, E. C.: Genesis of hummocks in glaciofluvial corridors near the Keewatin Ice Divide, Canada, Boreas, 38, 471–481, 2009.

Van Boeckel, M., Van Boeckel, T., and Hall, A. M.: Late erosion pulse triggered by rapid melt in the cold-based interior of the last Fennoscandian Ice Sheet, an example from Rogen, Earth Surface Processes and Landforms, 47, 3376–3394, 2022.

https://doi.org/10.5194/egusphere-2023-2141
Preprint. Discussion started: 16 October 2023

van den Broeke, M., Bus, C., Ettema, J., and Smeets, P.: Temperature thresholds for degree-day modelling of Greenland ice sheet melt rates, Geophysical Research Letters, 37, 2010.

Vérité, J., Ravier, É., Bourgeois, O., Bessin, P., Livingstone, S. J., Clark, C. D., Pochat, S., and Mourgues, R.: Formation of murtoos by repeated flooding of ribbed bedforms along subglacial meltwater corridors, Geomorphology, 408, 108 248, 2022.

Wake, L. and Marshall, S.: Assessment of current methods of positive degree-day calculation using in situ observations from glaciated regions, Journal of Glaciology, 61, 329–344, 2015.

Walder, J. S. and Fowler, A.: Channelized subglacial drainage over a deformable bed, Journal of glaciology, 40, 3–15, 1994.

Wallis, B. J., Hogg, A. E., van Wessem, J. M., Davison, B. J., and van den Broeke, M. R.: Widespread seasonal speed-up of west Antarctic Peninsula glaciers from 2014 to 2021, Nature Geoscience, 16, 231–237, 2023.

Weertman, J.: General theory of water flow at the base of a glacier or ice sheet, Reviews of Geophysics, 10, 287–333, 1972.

Werder, M. A., Hewitt, I. J., Schoof, C. G., and Flowers, G. E.: Modeling channelized and distributed subglacial drainage in two dimensions, Journal of Geophysical Research: Earth Surface, 118, 2140–2158, 2013.

Willis, I. C., Richards, K. S., and Sharp, M. J.: Links between proglacial stream suspended sediment dynamics, glacier hydrology and glacier motion at Midtdalsbreen, Norway, Hydrological Processes, 10, 629–648, 1996.

Yang, K. and Smith, L. C.: Internally drained catchments dominate supraglacial hydrology of the southwest Greenland Ice Sheet, Journal of Geophysical Research: Earth Surface, 121, 1891–1910, 2016.

https://doi.org/10.5194/egusphere-2023-2141
Preprint. Discussion started: 16 October 2023

Appendix A: Contents

This file contains supplementary information for '*Reorganisation of subglacial drainage processes during rapid melting of the Fennoscandian Ice Sheet*'

Movie A1. Evolution of the system with respect to overburden$_{\%}$ through time in the baseline model run. Model years 15–17 were arbitrarily chosen to illustrate the transient state of the system through several melt season cycles. Channels are shown as black lines where discharge exceeds $1\,\mathrm{m^3\,s^{-1}}$.

Figure A1. The distribution of meltwater routes, murtoo routes, and sediment in the Finnish Lake District Ice Lobe. **A)** Meltwater routes and murtoo routes as mapped by Ahokangas et al. (2021). There is a general absence of murtoos in the centre of the lobe 40–60 km from the ice margin. **B)** Sediment cover (GTK, Finland, 2010) showing thin sediment thickness in the terrain from which murtoos appear absent.

Figure A2. Median overburden$_{\%}$, channel discharge, Q_c, and sheet discharge, q_s over the full length of the baseline model run.

Figure A3–A31. Comparison of the median summer system for the range of sensitivity parameters against the baseline model run. **A**) Water pressure expressed as a percentage of overburden pressure, overburden$_{\%}$. Channels are shown as black lines where median discharge exceeds $1\,\mathrm{m^3\,s^{-1}}$. **B**) Baseline median summer overburden$_{\%}$ minus the tested median summer overburden$_{\%}$. The same figure caption applies for Figures A3–A31.

Figure A32. Boxplots of model parameters grouped by month for overburden (overburden$_{\%}$, **A**), sheet discharge (q_s, **B**), water velocity (V_W, **C**), and channel discharge (Q_c, **D**) during all model years at nodes between 40–60 km from the ice margin. As in Figure 4, nodes that fall within meltwater routes which do host murtoos (Murtoo free MRs) are shown in blue, nodes which fall within mapped meltwater routes that do not contain murtoo fields (Murtoo hosting MRs) are shown in orange, and all other nodes are shown in purple. Medians for each group are shown as black circles, and 'outliers'—defined as points more than 150% of the interquartile range away from the upper and lower quartile—are shown as crosses.

Tables A1–A4. Tukey-Kramer HSD test results for overburden$_{\%}$ (Table A1), q_s (Table A2), Q_c (Table A3), and V_w (Table A4) in meltwater routes, murtoo routes, and non-meltwater routes between 40–60 km from the ice margin. The upper and lower limits describe the 95% confidence intervals for the true mean difference, A-B is the difference between group means.

https://doi.org/10.5194/egusphere-2023-2141
Preprint. Discussion started: 16 October 2023

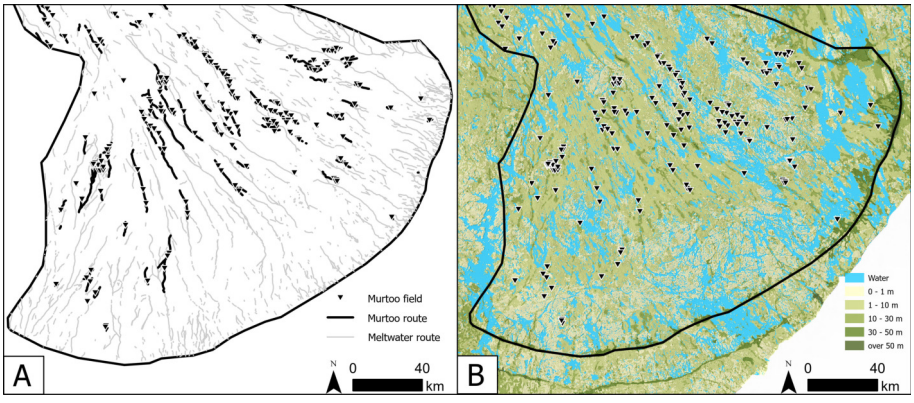

Figure A1. The distribution of meltwater routes, murtoo routes, and sediment in the Finnish Lake District Ice Lobe. **A)** Meltwater routes and murtoo routes as mapped by Ahokangas et al. (2021). There is a general absence of murtoos in the centre of the lobe 40–60 km from the ice margin. **B)** Sediment cover (GTK, Finland, 2010) showing thin sediment thickness in the terrain from which murtoos appear absent.

https://doi.org/10.5194/egusphere-2023-2141
Preprint. Discussion started: 16 October 2023

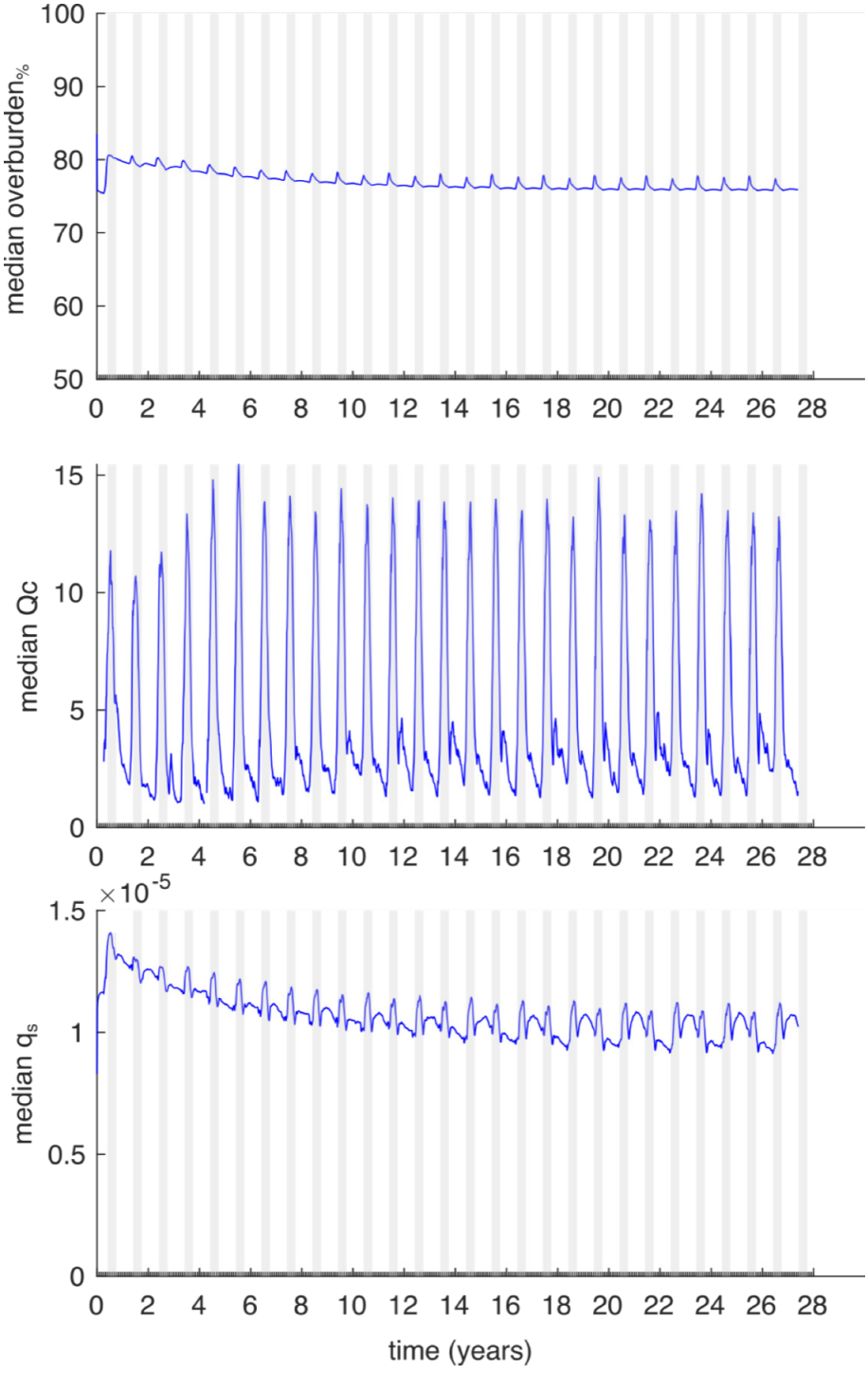

Figure A2. Median overburden$_{\%}$, channel discharge, Q_c, and sheet discharge, q_s over the full length of the baseline model run.

https://doi.org/10.5194/egusphere-2023-2141
Preprint. Discussion started: 16 October 2023

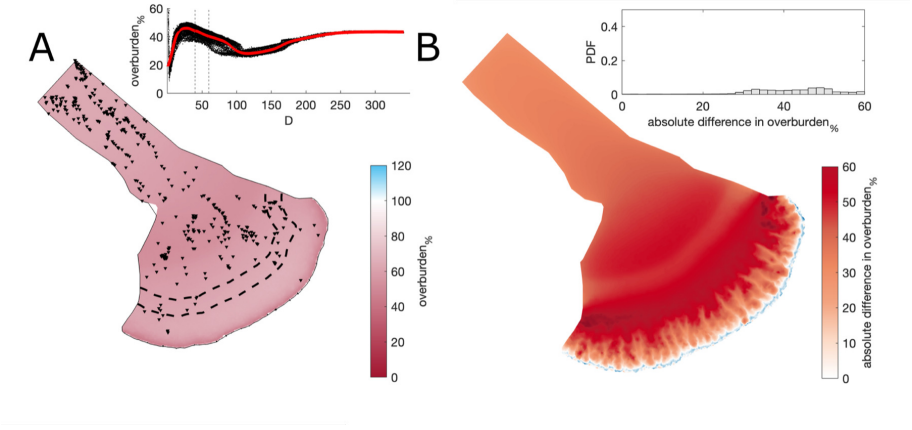

Figure A3. Comparison of the median summer system for sheet conductivity, $k_s = 10^{-2}\,\mathrm{m}^{7/4}\,\mathrm{kg}^{-1/2}$ against the baseline model run ($k_s = 10^{-4}\,\mathrm{m}^{7/4}\,\mathrm{kg}^{-1/2}$). **A**) Water pressure expressed as a percentage of overburden pressure, overburden$_{\%}$. Channels are shown as black lines where median discharge exceeds $1\,\mathrm{m}^3\,\mathrm{s}^{-1}$. **B**) Baseline median summer overburden$_{\%}$ minus the $k_s = 10^{-2}\,\mathrm{m}^{7/4}\,\mathrm{kg}^{-1/2}$ median summer overburden$_{\%}$. The same figure caption applies for Figures A3–A31

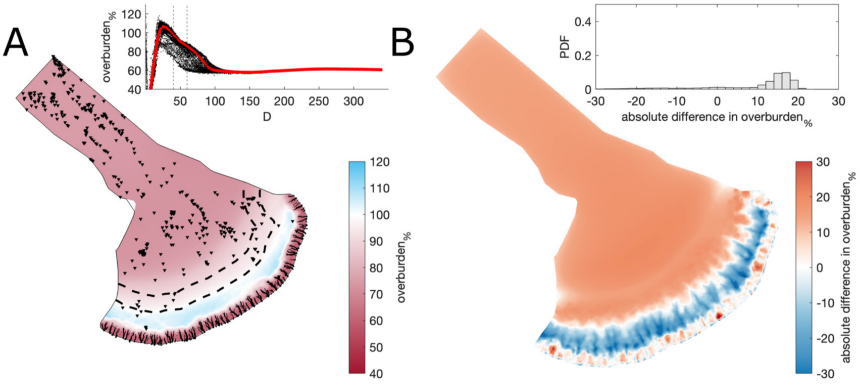

Figure A4. Comparison of the median summer system for sheet conductivity, $k_s = 10^{-3}\,\mathrm{m}^{7/4}\,\mathrm{kg}^{-1/2}$ against the baseline model run ($k_s = 10^{-4}\,\mathrm{m}^{7/4}\,\mathrm{kg}^{-1/2}$). The same figure caption as Figure A3 applies.

https://doi.org/10.5194/egusphere-2023-2141
Preprint. Discussion started: 16 October 2023

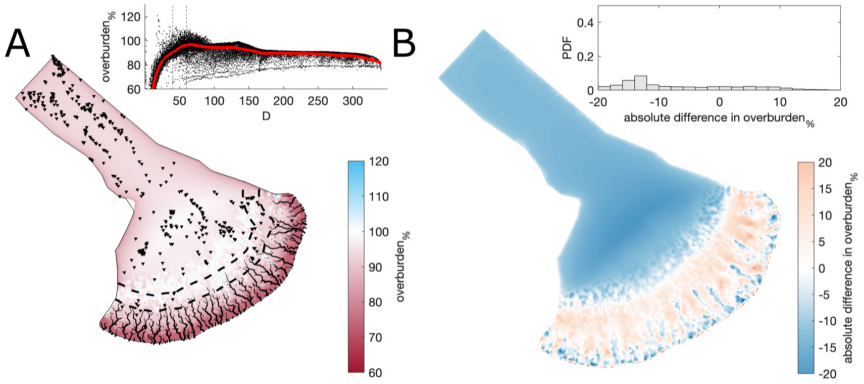

Figure A5. Comparison of the median summer system for sheet confuctivity, $k_s = 10^{-5}\,\mathrm{m}^{7/4}\,\mathrm{kg}^{-1/2}$ against the baseline model run ($k_s = 10^{-4}\,\mathrm{m}^{7/4}\,\mathrm{kg}^{-1/2}$). The same figure caption as Figure A3 applies.

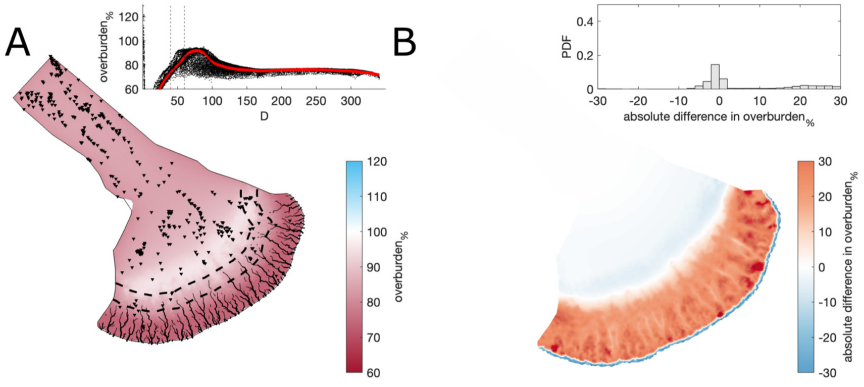

Figure A6. Comparison of the median summer system for channel conductivity, $k_c = 5 \times 10^{-1}\,\mathrm{m}^{3/2}\,\mathrm{kg}^{-1/2}$ against the baseline model run ($k_c = 10^{-1}\,\mathrm{m}^{3/2}\,\mathrm{kg}^{-1/2}$). The same figure caption as Figure A3 applies.

https://doi.org/10.5194/egusphere-2023-2141
Preprint. Discussion started: 16 October 2023

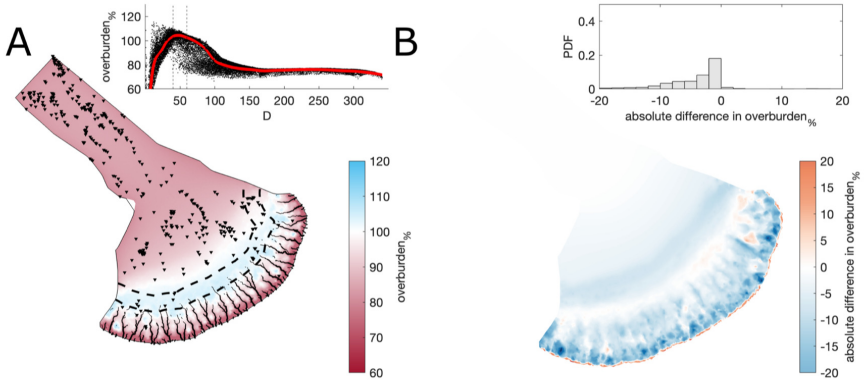

Figure A7. Comparison of the median summer system for channel conductivity, $k_c = 5 \times 10^{-2}\,\mathrm{m}^{3/2}\,\mathrm{kg}^{-1/2}$ against the baseline model run ($k_c = 10^{-1}\,\mathrm{m}^{3/2}\,\mathrm{kg}^{-1/2}$). The same figure caption as Figure A3 applies.

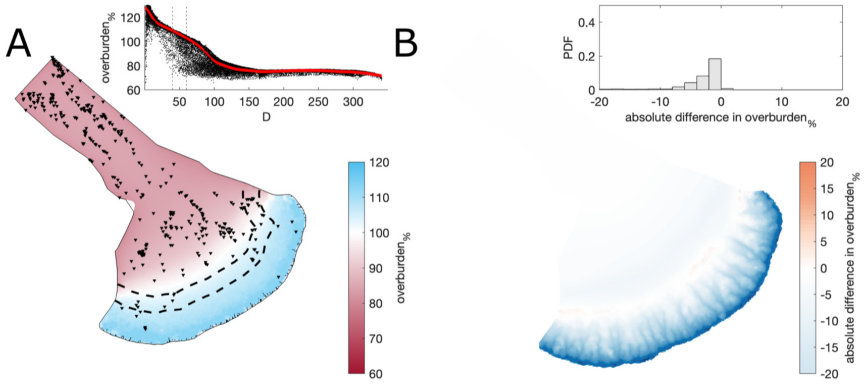

Figure A8. Comparison of the median summer system for channel conductivity, $k_c = 10^{-3}\,\mathrm{m}^{3/2}\,\mathrm{kg}^{-1/2}$ against the baseline model run ($k_c = 10^{-1}\,\mathrm{m}^{3/2}\,\mathrm{kg}^{-1/2}$). The same figure caption as Figure A3 applies.

https://doi.org/10.5194/egusphere-2023-2141
Preprint. Discussion started: 16 October 2023

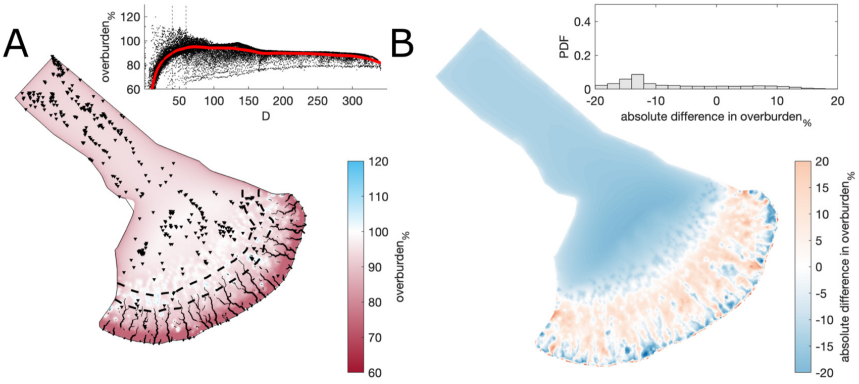

Figure A9. Comparison of the median summer system for moulin frequency, $N_{moulins} = 1000$ against the baseline model run ($N_{moulins} = 2500$). The same figure caption as Figure A3 applies.

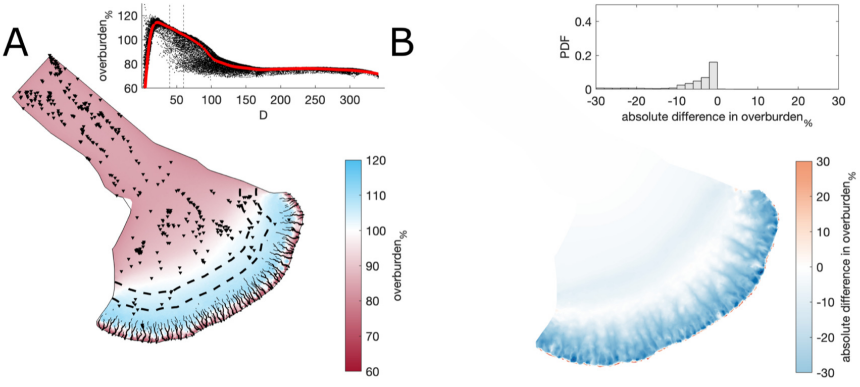

Figure A10. Comparison of the median summer system for moulin frequency, $N_{moulins} = 4000$ against the baseline model run ($N_{moulins} = 2500$). The same figure caption as Figure A3 applies.

https://doi.org/10.5194/egusphere-2023-2141
Preprint. Discussion started: 16 October 2023

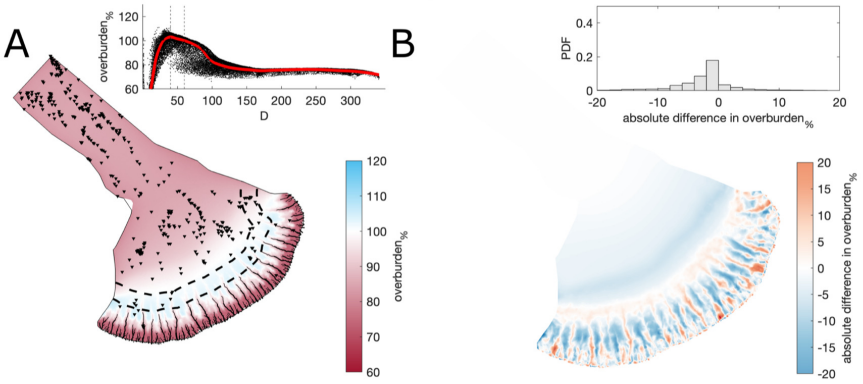

Figure A11. Comparison of the median summer system for where water was directly input at every nodes against the baseline model run ($N_{moulins} = 2500$). The same figure caption as Figure A3 applies.

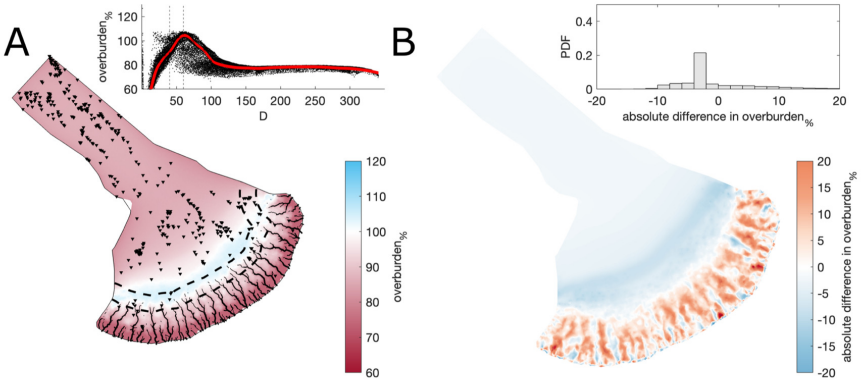

Figure A12. Comparison of the median summer system for a second random distribution of moulin frequency, $N_{moulins} = 2500$ against the baseline model run ($N_{moulins} = 2500$). The same figure caption as Figure A3 applies.

https://doi.org/10.5194/egusphere-2023-2141
Preprint. Discussion started: 16 October 2023

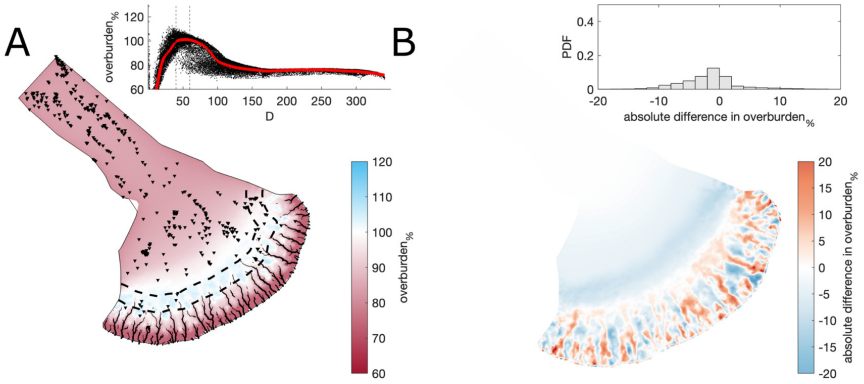

Figure A13. Comparison of the median summer system for a third random distribution of moulin frequency, $N_{moulins} = 2500$ against the baseline model run ($N_{moulins} = 2500$). The same figure caption as Figure A3 applies.

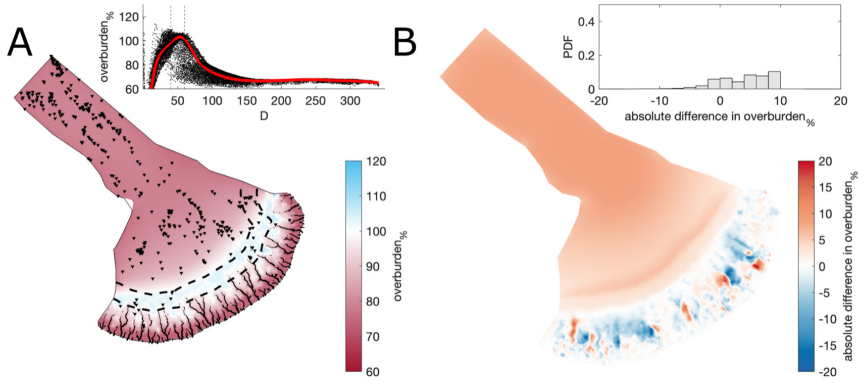

Figure A14. Comparison of the median summer system for basal melt rate, $b_{melt} = 1 \times 10^{-3}\,\mathrm{m\,yr{-}1}$ against the baseline model run ($b_{melt} = 1 \times 10^{-3}\mathrm{m\,yr{-}1}$). The same figure caption as Figure A3 applies.

https://doi.org/10.5194/egusphere-2023-2141
Preprint. Discussion started: 16 October 2023

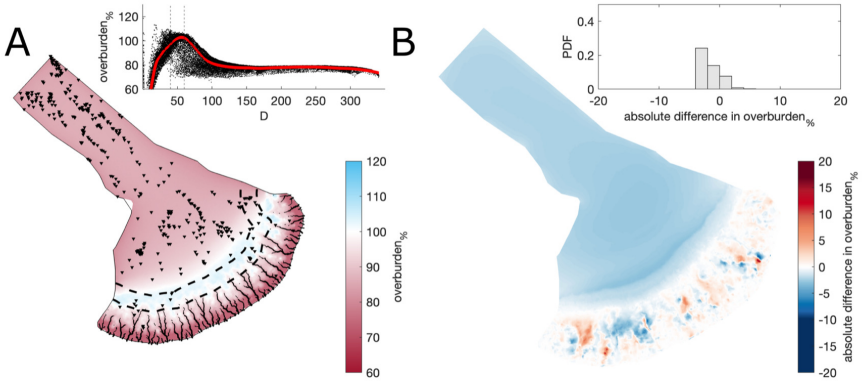

Figure A15. Comparison of the median summer system for basal melt rate, $b_{melt} = 1 \times 10^{-3}\,\mathrm{m\,yr{-}1}$ against the baseline model run ($b_{melt} = 7 \times 10^{-3}\,\mathrm{m\,yr{-}1}$). The same figure caption as Figure A3 applies.

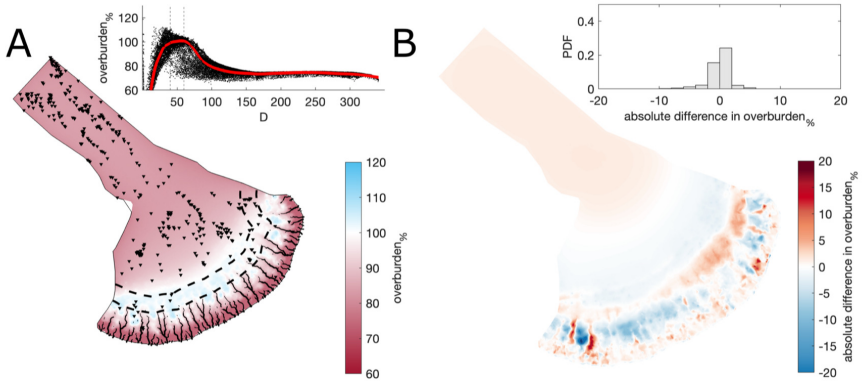

Figure A16. Comparison of the median summer system for basal bump height, $h_r = 0.1\,\mathrm{m}$ against the baseline model run ($h_r = 0.085\,\mathrm{m}$). The same figure caption as Figure A3 applies.

https://doi.org/10.5194/egusphere-2023-2141
Preprint. Discussion started: 16 October 2023

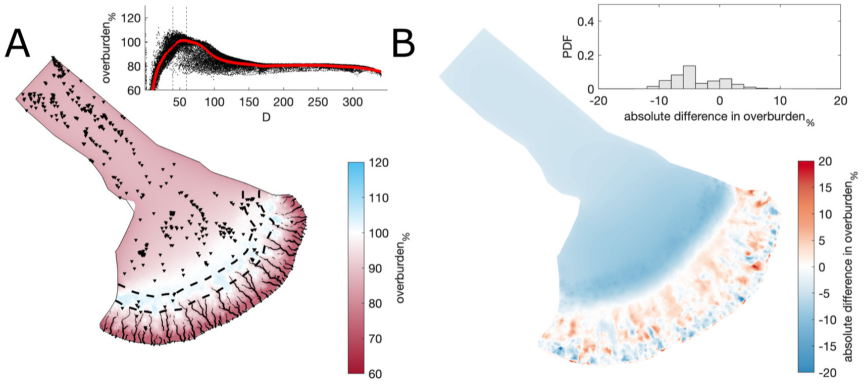

Figure A17. Comparison of the median summer system for basal bump height, $h_r = 0.05\,\mathrm{m}$ against the baseline model run ($h_r = 0.085\,\mathrm{m}$). The same figure caption as Figure A3 applies.

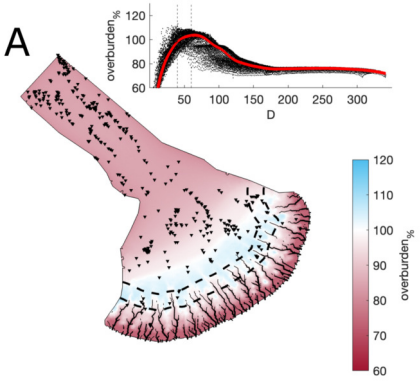

Figure A18. Comparison of a mesh that is not refined with respect to elevation against the baseline model run. The same figure caption as Figure A3 applies.

https://doi.org/10.5194/egusphere-2023-2141
Preprint. Discussion started: 16 October 2023

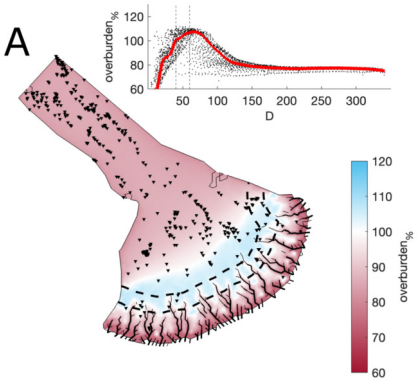

Figure A19. Comparison of a coarser mesh (edge length ∼5 km) against the baseline model run. The same figure caption as Figure A3 applies.

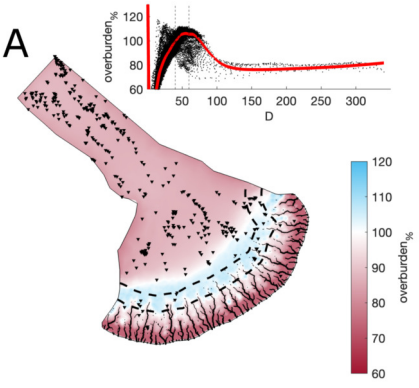

Figure A20. Comparison of a refined mesh (minimum edge length ≈300 m) <80 km from the ice margin against the baseline model run. The same figure caption as Figure A3 applies.

https://doi.org/10.5194/egusphere-2023-2141
Preprint. Discussion started: 16 October 2023

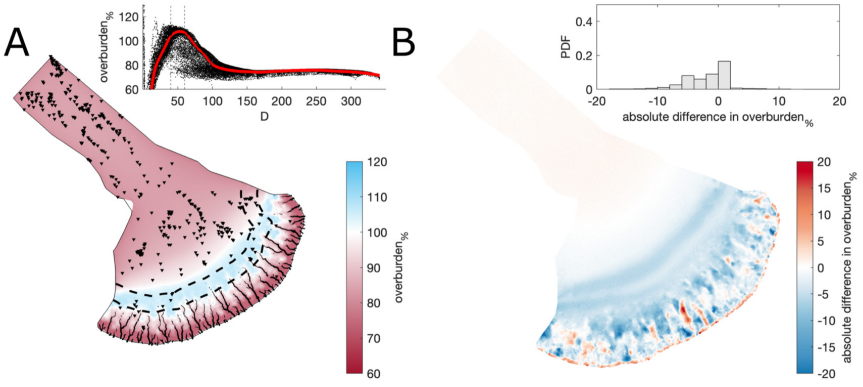

Figure A21. Comparison of a flat bed against the baseline model run. The same figure caption as Figure A3 applies.

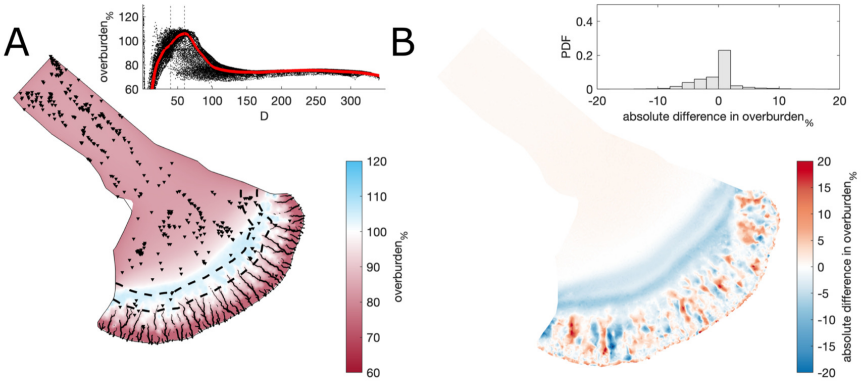

Figure A22. Comparison of a modern mesh (without subtracting Quaternary sediment thickness) against the baseline model run. The same figure caption as Figure A3 applies.

https://doi.org/10.5194/egusphere-2023-2141
Preprint. Discussion started: 16 October 2023

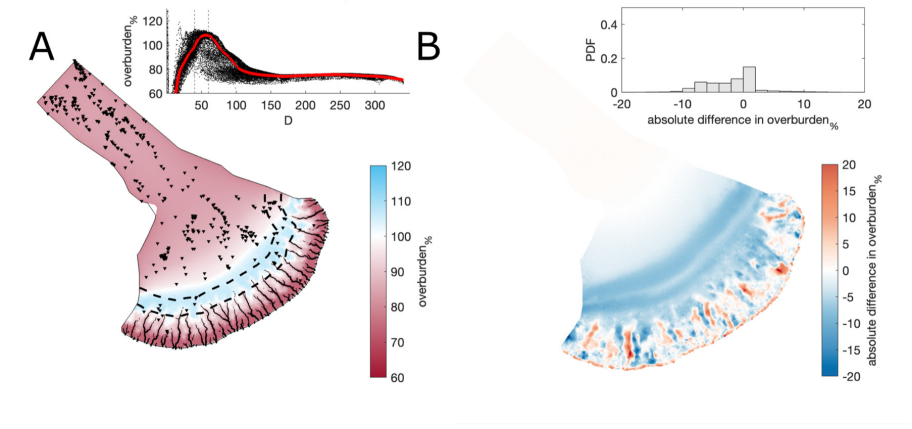

Figure A23. Comparison including lake bathymetry against the baseline model run. The same figure caption as Figure A3 applies.

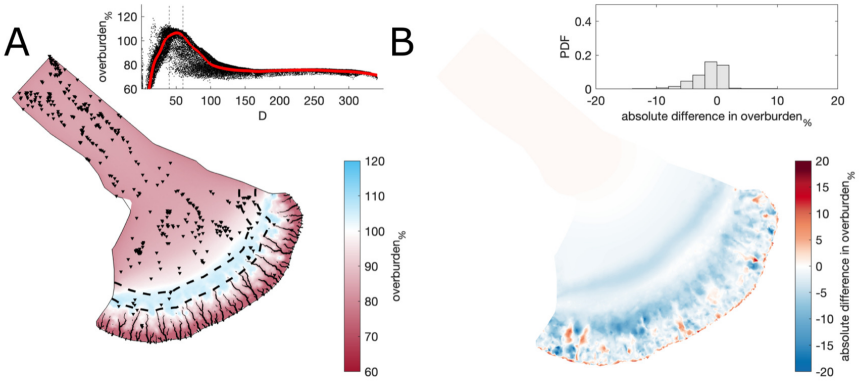

Figure A24. Comparison of a 30 m deep water body at the ice margin boundary against the baseline model run (land-terminating). The same figure caption as Figure A3 applies.

https://doi.org/10.5194/egusphere-2023-2141
Preprint. Discussion started: 16 October 2023

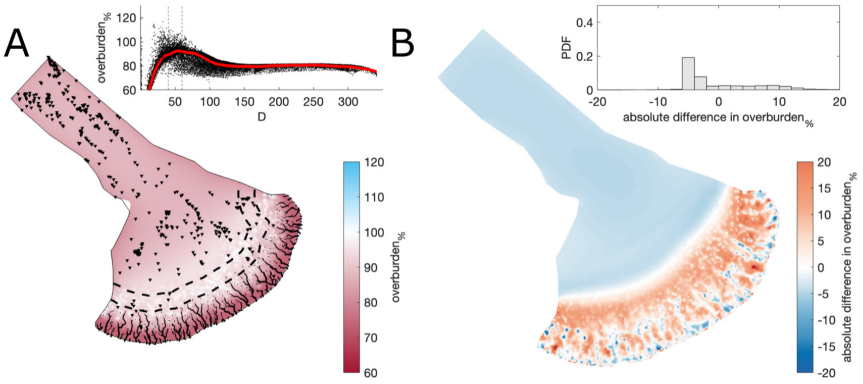

Figure A25. Comparison of the median summer system for an englacial void ratio, $E_{vr} = 10^{-3}$ against the baseline model run ($E_{vr} = 10^{-4}$). The same figure caption as Figure A3 applies.

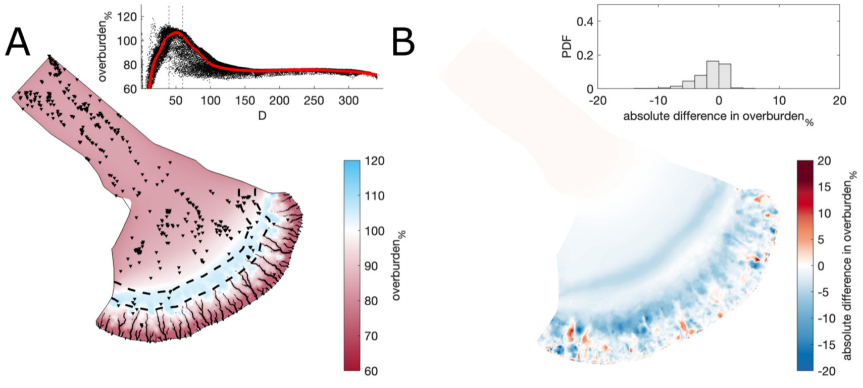

Figure A26. Comparison of the median summer system for an englacial void ratio, $E_{vr} = 10^{-5}$ against the baseline model run ($E_{vr} = 10^{-4}$). The same figure caption as Figure A3 applies.

https://doi.org/10.5194/egusphere-2023-2141
Preprint. Discussion started: 16 October 2023

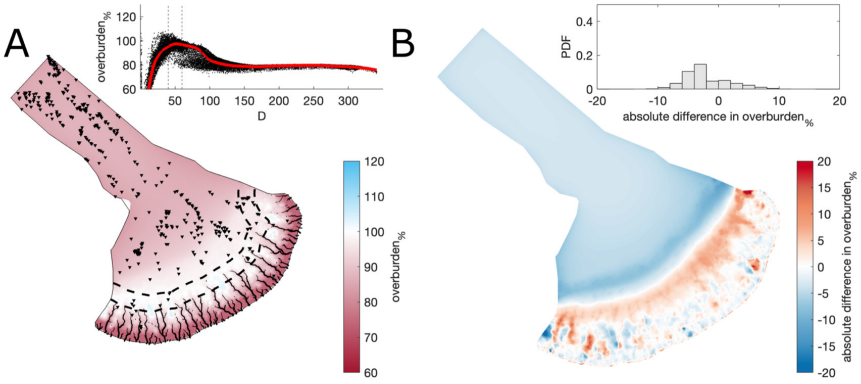

Figure A27. Comparison of the median summer system for a fixed velocity, $U_b = 100\,\mathrm{m\,yr{-}1}$ against the baseline model run ($U_b = 150\,\mathrm{m\,yr{-}1}$). The same figure caption as Figure A3 applies.

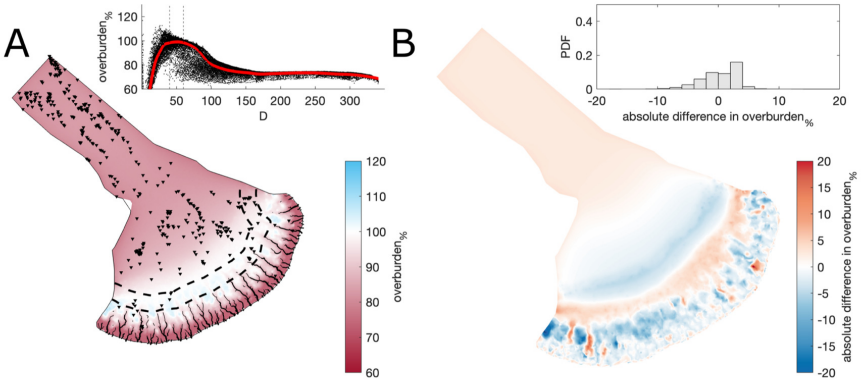

Figure A28. Comparison of the median summer system for a fixed velocity, $U_b = 200\,\mathrm{m\,yr{-}1}$ against the baseline model run ($U_b = 150\,\mathrm{m\,yr{-}1}$). The same figure caption as Figure A3 applies.

https://doi.org/10.5194/egusphere-2023-2141
Preprint. Discussion started: 16 October 2023

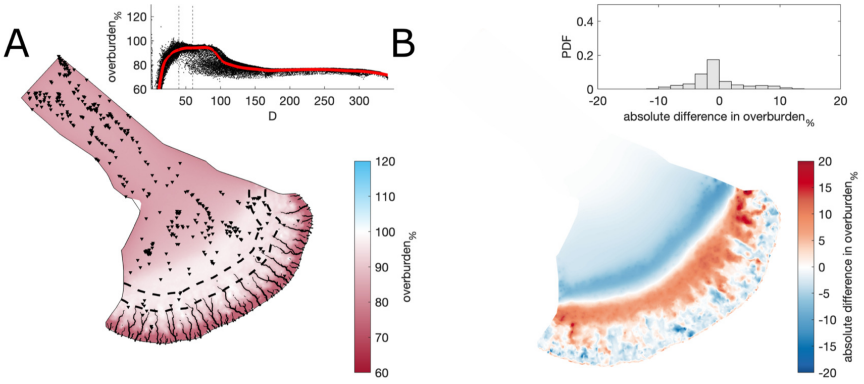

Figure A29. Comparison of the median summer system for a transient velocity, U_b with a median $U_b = 150\,\mathrm{m\,yr{-}1}$ against the fixed baseline model run ($U_b = 150\,\mathrm{m\,yr{-}1}$). The same figure caption as Figure A3 applies.

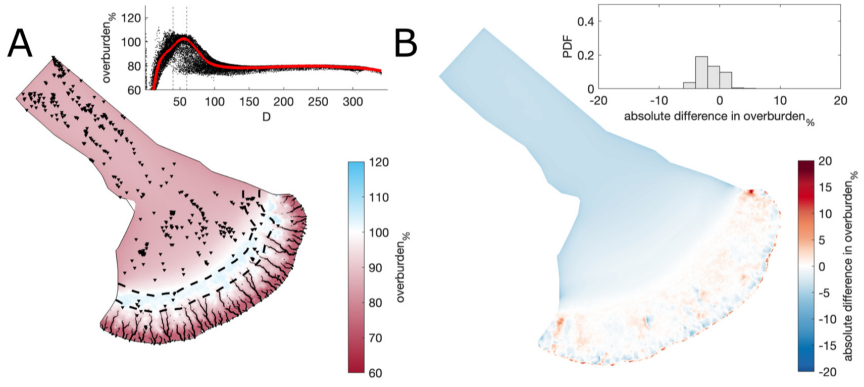

Figure A30. Comparison of the median summer system for a transient velocity, U_b with a median $U_b = 100\,\mathrm{m\,yr{-}1}$ against the fixed baseline model run ($U_b = 150\,\mathrm{m\,yr{-}1}$). The same figure caption as Figure A3 applies.

https://doi.org/10.5194/egusphere-2023-2141
Preprint. Discussion started: 16 October 2023

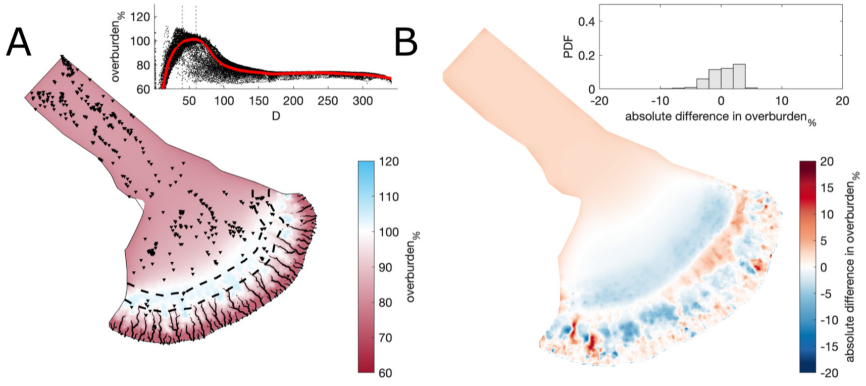

Figure A31. Comparison of the median summer system for a transient velocity, U_b with a median $U_b = 200\,\mathrm{m\,yr{-}1}$ against the fixed baseline model run ($U_b = 150\,\mathrm{m\,yr{-}1}$). The same figure caption as Figure A3 applies.

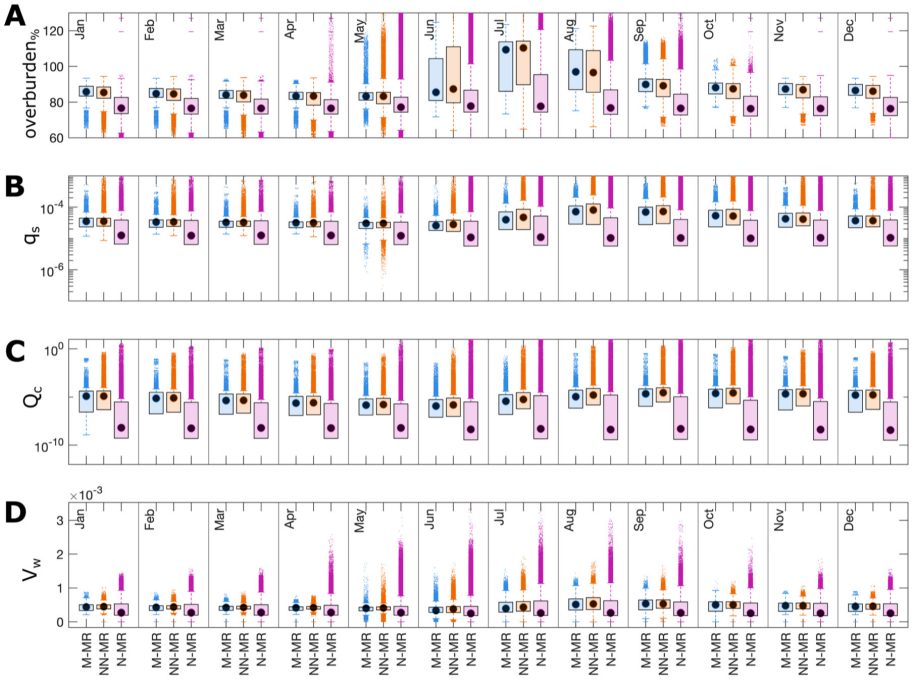

Figure A32. Boxplots of model parameters grouped by month for overburden (overburden$_{\%}$, **A**), sheet discharge (q_s, **B**), water velocity (V_W, **C**), and channel discharge (Q_c, **D**) during all model years at nodes between 40–60 km from the ice margin. As in Figure 4, nodes that fall within meltwater routes which do host murtoos (Murtoo free MRs) are shown in blue, nodes which fall within mapped meltwater routes that do not contain murtoo fields (Murtoo hosting MRs) are shown in orange, and all other nodes are shown in purple. Medians for each group are shown as black circles, and 'outliers'—defined as points more than 150% of the interquartile range away from the upper and lower quartile—are shown as crosses.

https://doi.org/10.5194/egusphere-2023-2141
Preprint. Discussion started: 16 October 2023

Table A1. Tukey-Kramer HSD test of overburden$_{\%}$ in meltwater routes, murtoo routes, and non-meltwater routes between 40–60 km from the ice margin. The upper and lower limits describe the 95% confidence intervals for the true mean difference, A-B is the difference between group means.

Month	Group A	Group B	Lower Limit	A-B	Upper limit	P-Value
	meltwater route	murtoo route	-1.71	-1.30	-0.89	0.00
January	non meltwater route	murtoo route	-10.49	-10.12	-9.75	0.00
	meltwater route	non meltwater route	8.58	8.82	9.06	0.00
	meltwater route	murtoo route	-1.62	-1.21	-0.80	0.00
February	non meltwater route	murtoo route	-9.87	-9.50	-9.12	0.00
	meltwater route	non meltwater route	8.05	8.29	8.52	0.00
	meltwater route	murtoo route	-1.58	-1.17	-0.76	0.00
March	non meltwater route	murtoo route	-9.30	-8.93	-8.55	0.00
	meltwater route	non meltwater route	7.52	7.75	7.99	0.00
	meltwater route	murtoo route	-1.55	-1.14	-0.73	0.00
April	non meltwater route	murtoo route	-8.33	-7.96	-7.58	0.00
	meltwater route	non meltwater route	6.58	6.82	7.06	0.00
	meltwater route	murtoo route	-1.10	-0.69	-0.28	0.00
May	non meltwater route	murtoo route	-5.26	-4.89	-4.51	0.00
	meltwater route	non meltwater route	3.96	4.20	4.43	0.00
	meltwater route	murtoo route	0.70	1.12	1.54	0.00
June	non meltwater route	murtoo route	-8.56	-8.17	-7.79	0.00
	meltwater route	non meltwater route	9.05	9.30	9.54	0.00
	meltwater route	murtoo route	0.10	0.52	0.93	0.00
July	non meltwater route	murtoo route	-18.72	-18.34	-17.96	0.00
	meltwater route	non meltwater route	18.61	18.85	19.10	0.00
	meltwater route	murtoo route	-2.01	-1.59	-1.18	0.00
August	non meltwater route	murtoo route	-18.81	-18.43	-18.04	0.00
	meltwater route	non meltwater route	16.59	16.83	17.08	0.00
	meltwater route	murtoo route	-2.30	-1.88	-1.47	0.00
September	non meltwater route	murtoo route	-14.47	-14.09	-13.71	0.00
	meltwater route	non meltwater route	11.97	12.21	12.45	0.00
	meltwater route	murtoo route	-2.14	-1.72	-1.31	0.00
October	non meltwater route	murtoo route	-12.49	-12.11	-11.73	0.00
	meltwater route	non meltwater route	10.15	10.39	10.63	0.00
	meltwater route	murtoo route	-1.99	-1.57	-1.15	0.00
November	non meltwater route	murtoo route	-12.06	-11.68	-11.30	0.00
	meltwater route	non meltwater route	9.87	10.11	10.36	0.00
	meltwater route	murtoo route	-1.88	-1.46	-1.04	0.00
December	non meltwater route	murtoo route	-11.56	-11.17	-10.79	0.00
	meltwater route	non meltwater route	9.47	9.72	9.96	0.00

https://doi.org/10.5194/egusphere-2023-2141
Preprint. Discussion started: 16 October 2023

Table A2. Tukey-Kramer HSD test of q_s in meltwater routes, murtoo routes, and non-meltwater routes between 40–60 km from the ice margin. The upper and lower limits describe the 95% confidence intervals for the true mean difference, A-B is the difference between group means.

Month	Group A	Group B	Lower Limit	A-B	Upper limit	P-Value
January	meltwater route	murtoo route	-5.07×10^{-7}	2.89×10^{-6}	6.28×10^{-6}	0.27
	non meltwater route	murtoo route	-1.57×10^{-5}	-1.26×10^{-5}	-9.54×10^{-7}	0.00
	meltwater route	non meltwater route	1.36×10^{-5}	1.55×10^{-5}	1.75×10^{-5}	0.00
February	meltwater route	murtoo route	-1.23×10^{-6}	2.19×10^{-6}	5.6×10^{-6}	0.88
	non meltwater route	murtoo route	-1.39×10^{-5}	-1.08×10^{-5}	-7.69×10^{-6}	0.00
	meltwater route	non meltwater route	1.1×10^{-5}	1.3×10^{-5}	1.5×10^{-5}	0.00
March	meltwater route	murtoo route	-2.05×10^{-6}	1.36×10^{-6}	4.77×10^{-6}	0.99
	non meltwater route	murtoo route	-1.26×10^{-5}	-9.49×10^{-6}	-6.37×10^{-6}	0.00
	meltwater route	non meltwater route	8.86×10^{-6}	1.08×10^{-5}	1.28×10^{-5}	0.00
April	meltwater route	murtoo route	-2.66×10^{-6}	7.6×10^{-7}	4.18×10^{-6}	0.99
	non meltwater route	murtoo route	-1.14×10^{-5}	-8.28×10^{-6}	-5.15×10^{-6}	0.00
	meltwater route	non meltwater route	7.05×10^{-6}	9.04×10^{-6}	1.10×10^{-5}	0.00
May	meltwater route	murtoo route	-2.92×10^{-6}	4.99×10^{-7}	3.92×10^{-6}	0.99
	non meltwater route	murtoo route	-7.11×10^{-6}	-3.98×10^{-6}	-8.53×10^{-5}	0.00
	meltwater route	non meltwater route	2.49×10^{-6}	4.48×10^{-6}	6.47×10^{-6}	0.00
June	meltwater route	murtoo route	9.57×10^{-7}	4.46×10^{-6}	7.97×10^{-6}	0.00
	non meltwater route	murtoo route	6.04×10^{-6}	9.25×10^{-6}	1.25×10^{-5}	0.00
	meltwater route	non meltwater route	-6.83×10^{-6}	-4.79×10^{-6}	-2.75×10^{-6}	0.00
July	meltwater route	murtoo route	1.36×10^{-5}	1.7×10^{-5}	2.05×10^{-5}	0.00
	non meltwater route	murtoo route	9.95×10^{-6}	1.31×10^{-5}	1.63×10^{-5}	0.00
	meltwater route	non meltwater route	1.89×10^{-6}	3.9×10^{-6}	5.91×10^{-6}	0.00
August	meltwater route	murtoo route	1.82×10^{-5}	2.17×10^{-5}	2.52×10^{-5}	0.00
	non meltwater route	murtoo route	-9.99×10^{-6}	-6.79×10^{-6}	-3.59×10^{-6}	0.00
	meltwater route	non meltwater route	2.65×10^{-5}	2.85×10^{-5}	3.05×10^{-5}	0.00
September	meltwater route	murtoo route	1.06×10^{-5}	1.41×10^{-5}	1.75×10^{-5}	0.00
	non meltwater route	murtoo route	-2.33×10^{-5}	-2.02×10^{-5}	1.7×10^{-5}	0.00
	meltwater route	non meltwater route	3.22×10^{-5}	3.42×10^{-5}	3.62×10^{-5}	0.00
October	meltwater route	murtoo route	5.67×10^{-6}	9.15×10^{-6}	1.26×10^{-5}	0.00
	non meltwater route	murtoo route	-2.44×10^{-5}	-2.12×10^{-5}	-1.8×10^{-5}	0.00
	meltwater route	non meltwater route	2.84×10^{-5}	3.04×10^{-5}	3.24×10^{-5}	0.00
November	meltwater route	murtoo route	2.52×10^{-6}	6×10^{-6}	9.48×10^{-6}	0.00
	non meltwater route	murtoo route	-2.14×10^{-5}	-1.82×10^{-5}	-1.50×10^{-5}	0.00
	meltwater route	non meltwater route	2.22×10^{-5}	2.42×10^{-5}	2.62×10^{-5}	0.00
December	meltwater route	murtoo route	7.23×10^{-7}	4.22×10^{-6}	7.71×10^{-6}	0.00
	non meltwater route	murtoo route	-1.87×10^{-5}	-1.55×10^{-5}	1.23×10^{-5}	0.00
	meltwater route	non meltwater route	1.77×10^{-5}	1.97×10^{-5}	2.18×10^{-5}	0.00

https://doi.org/10.5194/egusphere-2023-2141
Preprint. Discussion started: 16 October 2023

Table A3. Tukey-Kramer HSD test of Q_c in meltwater routes, murtoo routes, and non-meltwater routes between 40–60 km from the ice margin. The upper and lower limits describe the 95% confidence intervals for the true mean difference, A-B is the difference between group means.

Month	Group A	Group B	Lower Limit	A-B	Upper limit	P-Value
January	meltwater route	murtoo route	-7.57×10^{-3}	6.51×10^{-4}	8.87×10^{-3}	0.99
	non meltwater route	murtoo route	-6.19×10^{-3}	1.34×10^{-3}	8.86×10^{-3}	0.99
	meltwater route	non meltwater route	-5.47×10^{-3}	-6.86×10^{-4}	4.1×10^{-3}	0.99
February	meltwater route	murtoo route	-7.78×10^{-3}	5.08×10^{-4}	8.79×10^{-3}	0.99
	non meltwater route	murtoo route	-6.72×10^{-3}	5.08×10^{-4}	8.44×10^{-3}	0.99
	meltwater route	non meltwater route	-5.18×10^{-3}	-3.53×10^{-4}	4.47×10^{-3}	0.99
March	meltwater route	murtoo route	-7.86×10^{-3}	4.06×10^{-4}	8.677×10^{-3}	0.99
	non meltwater route	murtoo route	-6.93×10^{-3}	6.3×10^{-4}	8.19×10^{-3}	0.99
	meltwater route	non meltwater route	-5.04×10^{-3}	-2.24×10^{-4}	4.59×10^{-5}	0.99
April	meltwater route	murtoo route	-7.98×10^{-3}	3.07×10^{-4}	8.59×10^{-3}	0.99
	non meltwater route	murtoo route	-7.10×10^{-3}	4.83×10^{-4}	8.06×10^{-3}	0.99
	meltwater route	non meltwater route	-5×10^{-3}	-1.76×10^{-4}	4.65×10^{-3}	0.99
May	meltwater route	murtoo route	$-8{,}02\times10^{-3}$	$2{,}60\times10^{-4}$	$8{,}54\times10^{-3}$	0.99
	non meltwater route	murtoo route	$-5{,}58\times10^{-3}$	$2{,}01\times10^{-3}$	$9{,}59\times10^{-3}$	0.99
	meltwater route	non meltwater route	$-6{,}57\times10^{-3}$	$-1{,}75\times10^{-3}$	$3{,}08\times10^{-3}$	0.99
June	meltwater route	murtoo route	$-7{,}93\times10^{-3}$	$5{,}65\times10^{-4}$	$9{,}06\times10^{-3}$	0.99
	non meltwater route	murtoo route	$7{,}28\times10^{-3}$	$1{,}51\times10^{-2}$	$2{,}28\times10^{-2}$	0.00
	meltwater route	non meltwater route	$-1{,}94\times10^{-2}$	$-1{,}45\times10^{-2}$	$-9{,}54\times10^{-3}$	0.00
July	meltwater route	murtoo route	$-6{,}22\times10^{-3}$	$2{,}14\times10^{-3}$	$1{,}05\times10^{-2}$	0.99
	non meltwater route	murtoo route	$3{,}20\times10^{-2}$	$3{,}97\times10^{-2}$	$4{,}73\times10^{-2}$	0.00
	meltwater route	non meltwater route	$-4{,}24\times10^{-2}$	$-3{,}75\times10^{-2}$	$-3{,}27\times10^{-2}$	0.00
August	meltwater route	murtoo route	$-4{,}45\times10^{-3}$	$4{,}02\times10^{-3}$	$1{,}25\times10^{-2}$	0.99
	non meltwater route	murtoo route	$3{,}97\times10^{-2}$	$4{,}74\times10^{-2}$	$5{,}52\times10^{-2}$	0.00
	meltwater route	non meltwater route	$-4{,}84\times10^{-2}$	$-4{,}34\times10^{-2}$	$-3{,}85\times10^{-2}$	0.00
September	meltwater route	murtoo route	$-4{,}64\times10^{-3}$	$3{,}75\times10^{-3}$	$1{,}21\times10^{-2}$	0.99
	non meltwater route	murtoo route	$2{,}24\times10^{-2}$	$3{,}01\times10^{-2}$	$3{,}78\times10^{-2}$	0.00
	meltwater route	non meltwater route	$-3{,}12\times10^{-2}$	$-2{,}63\times10^{-2}$	$-2{,}15\times10^{-2}$	0.00
October	meltwater route	murtoo route	$-6{,}24\times10^{-3}$	$2{,}19\times10^{-3}$	$1{,}06\times10^{-2}$	0.99
	non meltwater route	murtoo route	$2{,}22\times10^{-3}$	$9{,}94\times10^{-3}$	$1{,}77\times10^{-2}$	0.00
	meltwater route	non meltwater route	$-1{,}27\times10^{-2}$	$-7{,}75\times10^{-3}$	$-2{,}84\times10^{-3}$	0.00
November	meltwater route	murtoo route	$-7{,}16\times10^{-3}$	$1{,}27\times10^{-3}$	$9{,}70\times10^{-3}$	0.99
	non meltwater route	murtoo route	$-4{,}08\times10^{-3}$	$3{,}63\times10^{-3}$	$1{,}13\times10^{-2}$	0.99
	meltwater route	non meltwater route	$-7{,}27\times10^{-3}$	$-2{,}36\times10^{-3}$	$2{,}55\times10^{-3}$	0.99
December	meltwater route	murtoo route	$-7{,}56\times10^{-3}$	$9{,}10\times10^{-4}$	$9{,}38\times10^{-3}$	0.99
	non meltwater route	murtoo route	$-5{,}57\times10^{-3}$	$2{,}18\times10^{-3}$	$9{,}94\times10^{-3}$	0.99
	meltwater route	non meltwater route	$-6{,}21\times10^{-3}$	$-1{,}27\times10^{-3}$	$3{,}66\times10^{-3}$	0.99

https://doi.org/10.5194/egusphere-2023-2141
Preprint. Discussion started: 16 October 2023

Table A4. Tukey-Kramer HSD test of V_W in meltwater routes, murtoo routes, and non-meltwater routes between 40–60 km from the ice margin. The upper and lower limits describe the 95% confidence intervals for the true mean difference, A-B is the difference between group means.

Month	Group A	Group B	Lower Limit	A-B	Upper limit	P-Value
January	meltwater route	murtoo route	1.41×10^{-6}	7.42×10^{-6}	1.34×10^{-5}	0.00
	non meltwater route	murtoo route	-5.63×10^{-5}	-5.08×10^{-5}	-4.53×10^{-5}	0.00
	meltwater route	non meltwater route	5.47×10^{-5}	5.82×10^{-5}	6.17×10^{-5}	0.00
Febuary	meltwater route	murtoo route	1.11×10^{-6}	7.17×10^{-6}	1.32×10^{-5}	0.00
	non meltwater route	murtoo route	-4.63×10^{-5}	-4.08×10^{-5}	-3.53×10^{-5}	0.00
	meltwater route	non meltwater route	4.44×10^{-5}	4.80×10^{-5}	5.15×10^{-5}	0.00
March	meltwater route	murtoo route	7.90×10^{-7}	6.83×10^{-6}	1.29×10^{-5}	0.01
	non meltwater route	murtoo route	-3.88×10^{-5}	-3.32×10^{-5}	-2.77×10^{-5}	0.00
	meltwater route	non meltwater route	3.65×10^{-5}	4.01×10^{-5}	4.36×10^{-5}	0.00
April	meltwater route	murtoo route	1.06×10^{-6}	7.11×10^{-6}	1.32×10^{-5}	0.00
	non meltwater route	murtoo route	-3.26×10^{-5}	-2.71×10^{-5}	-2.16×10^{-5}	0.00
	meltwater route	non meltwater route	3.07×10^{-5}	3.42×10^{-5}	3.77×10^{-5}	0.00
May	meltwater route	murtoo route	1.73×10^{-6}	7.78×10^{-6}	1.38×10^{-5}	0.00
	non meltwater route	murtoo route	-6.47×10^{-6}	-9.33×10^{-7}	4.61×10^{-6}	1.00
	meltwater route	non meltwater route	5.19×10^{-6}	8.72×10^{-6}	1.22×10^{-5}	0.00
June	meltwater route	murtoo route	1.22×10^{-5}	1.84×10^{-5}	2.46×10^{-5}	0.00
	non meltwater route	murtoo route	4.12×10^{-5}	4.69×10^{-5}	5.26×10^{-5}	0.00
	meltwater route	non meltwater route	-3.21×10^{-5}	-2.85×10^{-5}	-2.48×10^{-5}	0.00
July	meltwater route	murtoo route	2.47×10^{-5}	3.09×10^{-5}	3.70×10^{-5}	0.00
	non meltwater route	murtoo route	7.34×10^{-7}	6.33×10^{-6}	1.19×10^{-5}	0.01
	meltwater route	non meltwater route	2.10×10^{-5}	2.45×10^{-5}	2.81×10^{-5}	0.00
August	meltwater route	murtoo route	1.46×10^{-5}	2.08×10^{-5}	2.70×10^{-5}	0.00
	non meltwater route	murtoo route	-1.05×10^{-4}	-9.90×10^{-5}	-9.34×10^{-5}	0.00
	meltwater route	non meltwater route	1.16×10^{-4}	1.20×10^{-4}	1.23×10^{-4}	0.00
September	meltwater route	murtoo route	2.52×10^{-6}	8.65×10^{-6}	1.48×10^{-5}	0.00
	non meltwater route	murtoo route	-1.19×10^{-4}	-1.14×10^{-4}	-1.08×10^{-4}	0.00
	meltwater route	non meltwater route	1.19×10^{-4}	1.22×10^{-4}	1.26×10^{-4}	0.00
October	meltwater route	murtoo route	8.15×10^{-6}	1.43×10^{-5}	2.05×10^{-5}	0.00
	non meltwater route	murtoo route	-9.90×10^{-5}	-9.34×10^{-5}	-8.77×10^{-5}	0.00
	meltwater route	non meltwater route	1.04×10^{-4}	1.08×10^{-4}	1.11×10^{-4}	0.00
November	meltwater route	murtoo route	6.68×10^{-6}	1.28×10^{-5}	1.90×10^{-5}	0.00
	non meltwater route	murtoo route	-8.03×10^{-5}	-7.46×10^{-5}	-6.90×10^{-5}	0.00
	meltwater route	non meltwater route	8.39×10^{-5}	8.75×10^{-5}	9.10×10^{-5}	0.00
December	meltwater route	murtoo route	3.95×10^{-6}	1.01×10^{-5}	1.63×10^{-5}	0.00
	non meltwater route	murtoo route	-6.79×10^{-5}	-6.22×10^{-5}	-5.65×10^{-5}	0.00
	meltwater route	non meltwater route	6.87×10^{-5}	7.23×10^{-5}	7.59×10^{-5}	0.00